Glaciation of liquid clouds, snowfall and reduced cloud cover at industrial aerosol hot spots

Article

Accepted Version

Toll, V., Rahu, J., Keernik, H., Trofimov, H., Voormansik, T., Manshausen, P., Hung, E., Michelson, D., Christensen, M. W., Post, P., Junninen, H., Murray, B. J., Lohmann, U., Watson-Parris, D., Stier, P., Donaldson, N., Storelvmo, T., Kulmala, M. and Bellouin, N. ORCID: https://orcid.org/0000-0003-2109-9559 (2024) Glaciation of liquid clouds, snowfall and reduced cloud cover at industrial aerosol hot spots. Science, 386 (6723). pp. 756-762. ISSN 1095-9203 doi: 10.1126/science.adl0303 Available at https://centaur.reading.ac.uk/118984/

To link to this article DOI: http://dx.doi.org/10.1126/science.adl0303

Publisher: American Association for the Advancement of Science

Title: Glaciation of liquid clouds, snowfall and reduced cloud cover at industrial aerosol hot spots

Authors: Velle Toll[1]*, Jorma Rahu[1], Hannes Keernik[1], Heido Trofimov[1], Tanel Voormansik[1], Peter Manshausen[2], Emma Hung[3], Daniel Michelson[3], Matthew W. Christensen[4], Piia Post[1], Heikki Junninen[1], Benjamin J. Murray[5], Ulrike Lohmann[6], Duncan Watson-Parris[7], Philip Stier[2], Norman Donaldson[3], Trude Storelvmo[8], Markku Kulmala[9], Nicolas Bellouin[10]

Affiliations:

[1]Institute of Physics, University of Tartu; Tartu, Estonia.

[2]Department of Physics, University of Oxford; Oxford, UK.

[3]Environment and Climate Change Canada; Toronto, Canada.

[4]Atmospheric Science & Global Change Division, Pacific Northwest National Laboratory; Richland, Washington, USA.

[5]Institute for Climate and Atmospheric Science, School of Earth and Environment, University of Leeds; Leeds, UK.

[6]Institute of Atmospheric and Climate Science, ETH Zürich; Zürich, Switzerland.

[7]Scripps Institution of Oceanography and Halıcıoğlu Data Science Institute, University of California San Diego, USA.

[8]Department of Geosciences, University of Oslo; Oslo, Norway.

[9]Institute for Atmospheric and Earth System Research, University of Helsinki; Helsinki, Finland.

[10]Department of Meteorology, University of Reading; Reading, UK.

*Corresponding author. Email: velle.toll@ut.ee

Abstract: The ability of anthropogenic aerosols to freeze supercooled cloud droplets remains debated. Here, we present observational evidence for the glaciation of supercooled liquid-water clouds at industrial aerosol hot spots at temperatures between -10 and -24 °C. Compared to the nearby liquid-water clouds, the shortwave reflectance is reduced by 14% and longwave radiance increased by 4% in the glaciation-affected regions. There is an 8% reduction in cloud cover and an 18% reduction in cloud optical thickness. Additionally, daily glaciation-induced snowfall accumulations reach 15 mm. Glaciation events downwind industrial aerosol hot spots indicate that anthropogenic aerosols likely serve as ice-nucleating particles. However, rare glaciation events downwind of nuclear power plants indicate that factors other than aerosol emissions may also play a role in the observed glaciation events.

One-Sentence Summary: Supercooled cloud droplets transformed into ice crystals downwind strong anthropogenic air pollution sources.

Main Text: It remains uncertain to what extent anthropogenic aerosols, i.e. tiny air pollution particles, counteract global warming induced by anthropogenic greenhouse gases (*1*, *2*). Moreover, it remains unclear if, in addition to serving as cloud condensation nuclei (CCN), anthropogenic aerosols impact clouds and climate by serving as ice nucleating particles (INPs) (*3*-16). Supercooled liquid-water clouds exist in the Earth's atmosphere because INPs are required for ice nucleation at higher subzero temperatures than about -36 °C, but INPs are a rare subset of atmospheric aerosols (*3*).

Anthropogenic INPs have been suggested as one of the multiple possible reasons for the observed plume-shaped areas of anthropogenic snowfall downwind of industrial facilities (*17*–*20*). Such industrial facilities emit heat, water vapour, aerosol precursor gases and aerosol particles that could serve as CCN or INPs. Plume-shaped areas of snow downwind industrial facilities have been suggested to result directly from condensation cloud formed from the water vapour emitted by industry (*18*, *19*), due to the interaction of industrial emissions with supercooled fog below the stacks (*17*, *20*, *21*), from a seeder-feeder process when naturally occurring snow acts as seed for further snow in the industrial condensation cloud below (*22*) and from the impact of anthropogenic emissions on the cloud deck above (*18*). Here, we rely on remote sensing to study the impact of industrial emissions on the supercooled cloud decks above the stacks and identify which industrial sources lead to glaciation (detailed methods under supplementary Materials and Methods). We observe the glaciation of supercooled liquid-water clouds downwind of 67 anthropogenic aerosol hot spots, indicating that various industrial aerosols serve as INPs. At four sites, we also see glaciation downwind of nuclear power plants likely emitting little to no aerosols serving as INPs, indicating that factors other than INPs may also play a role in the observed glaciation events. However, it is also possible that buoyant plumes from the nuclear power plants loft nearby aerosols that serve as INPs.

Glaciation of liquid-water clouds at anthropogenic aerosol hot spots

We discovered glaciation events where supercooled liquid-phase clouds are converted into ice clouds near anthropogenic aerosol hot spots like metallurgical and cement industries, coal-fired power plants and oil refineries (Fig 1, S1, Movies S1 and S2) and, in five cases, downwind nuclear power plants (Fig S2). We identified 67 different aerosol sources leading to glaciation events (Table 1, Fig 2a, supplementary methods “Identification of glaciation events”) and 298 glaciation events at five aerosol sources studied in more detail over the years 2000 to 2021 (supplementary methods “Analysis of MODIS satellite data for selected aerosol sources”). To identify glaciation events, we detected plume-shaped areas of reduced cloud cover in the near-infrared composite satellite images from the Moderate Resolution Imaging Spectroradiometer (MODIS) instrument on board the Terra satellite. To identify the aerosol sources leading to glaciation, we used Google Maps. Using the National Aeronautics and Space Administration (NASA) Worldview interactive interface, we hand-logged the glaciation-affected regions at five aerosol sources for more detailed analysis.

Overlays of satellite data from polar-orbiting Terra MODIS and Geostationary Operational Environmental Satellite (GOES) Advanced Baseline Imager (ABI) with ground-based precipitation radar data reveal a causal sequence from glaciation to snowfall to reduced cloud cover (example in Movie S2). We infer the likely physical explanation for glaciation events (Fig 3) based on cloud perturbations at various aerosol sources and various products from remote sensing instruments (examples in Fig 1). In MODIS and GOES ABI data, we see ice clouds in the middle of the supercooled liquid-water cloud decks downwind of industrial aerosol sources (Fig 1a). We see snowfall in ground-based precipitation radar data (Fig 1b, S3 to S5, Movies S2 and S3), which is likely induced by the growth of ice crystals at the expense of supercooled cloud droplets because of the lower saturation pressure of water vapour over ice than over liquid water (*23*). And finally, we see reduced cloud cover in MODIS and GOES ABI data (Fig 1c, S1). At the same time, the plume-shaped areas of ice clouds, snowfall and reduced cloud cover overlap strikingly well (Fig S5, Movie S2).

Passive and active remote sensing of clouds and precipitation reveal both ice clouds in the middle of supercooled liquid-water clouds (Fig 1a) and glaciation-induced snowfall (Fig 1b). The glaciation-induced cloud perturbations identified in satellite data remain visible for 17 hours in GOES ABI images (supplementary methods “Analysis of GOES ABI satellite data”) and glaciation-induced snowfall events identified in ground-based precipitation radar data for 8 hours on average (supplementary methods “Analysis of ground-based precipitation radar data”). While the glaciation-induced cloud perturbations cover 4066 km^2, the plume-shaped areas of snow cover 2161 km^2 on average. Even though glaciation itself happens quickly and night-time identification of cloud phase from passive remote sensing is challenging (*24*), we identify ice clouds in the middle of supercooled liquid-water clouds in 69% of the cases studied using geostationary satellite data (supplementary methods “Analysis of GOES ABI satellite data”). Moreover, we observe plume-shaped snowfall areas in 29% of the studied cases where we have precipitation radar data available. For all the precipitating cases where we have dual-polarimetric radar data available, the hydrometeor classification identifies the type of precipitation as snow. Interestingly, in three cases, plume-shaped areas with fresh snow on the ground are seen in satellite data after the clouds have cleared away (example in Fig 1d). The glaciation-induced snowfall significantly affects precipitation amounts close to the studied industrial aerosol sources. Daily snowfall accumulations due to glaciation events reach 15 mm, while snowfall intensity is 1.2 mm/h on average (see supplementary methods “Analysis of ground-based precipitation radar data”).

Linking glaciation events to industrial emissions

Most of the identified glaciation events occur downwind of strong localised anthropogenic aerosol sources (Table 1). The cloud perturbations associated with glaciation events have a similar shape and spatial extent to CCN-polluted cloud tracks in liquid-water clouds (Fig S6; *25*, *26*). Both CCN perturbations on clouds and glaciation events have a characteristic head pointing towards the industrial point source, or the perturbation area is plume-shaped, indicating that the industrial source is inducing the observed cloud perturbation (Figs 1, S1 to S6). The widths of plume-shaped CCN perturbations on clouds and glaciation events are tens of kilometres and the lengths are hundreds of kilometres (Fig S6). Glaciation events occur under similar but colder meteorological conditions than CCN perturbations (Figs 4a and 4b, S7 to S9; *27–29*). Glaciation events are more frequent in colder months (November to February; Figs S10 and S11). Visual classification of cloud types indicates that both CCN perturbations and glaciation events occur in stratiform clouds (*26*; Fig 1, S1, S6). Based on atmospheric reanalysis and MODIS satellite data, glaciation events are seen more likely in high pressure situations with uniform stratiform cloud decks, high cloud fraction, average cloud water path around 184 g/m^2, low relative humidity above clouds and a statically stable lower troposphere (Figs 4b, S7 and S8; supplementary methods “Meteorological conditions favourable for glaciation events”). Such meteorological conditions have previously been found to be favourable for the occurrence of stratiform clouds susceptible to aerosols and for the formation of aerosol-induced cloud perturbations visible in MODIS satellite images (*28*). In addition, the plume-shaped glaciation events studied here are visually distinct from the oval-shaped aircraft-induced hole punch and canal clouds (Fig S6) and form under higher subzero temperatures compared to the hole punch clouds (Fig 4a). MODIS cloud top temperatures show that glaciation events occur mostly at temperatures between -10 to -24 °C (Fig 4a), but the characteristic cloud top temperatures vary depending on the aerosol source (Fig S9a). Downwind the cement plants in Volsk and Fokino, glaciation events occur at higher subzero temperatures compared to other sites (Figs S9a and S9b), but at Volsk and Fokino, the cloud top temperatures between about -15 °C and 0 °C are also in general more frequent in supercooled liquid-water cloud decks in winters (Fig S9c), where glaciation events mainly occur (Figs S10 and S11). At the temperatures characteristic of glaciation events, the adiabatic cooling down to homogeneous freezing temperatures is less likely compared to the conditions characteristic of the hole punch clouds at Moscow Domodedovo airport (Fig 4a) situated in Eastern Europe between the studied sites at Fokino and Cherepovets. However, hole punch clouds can also occur at higher subzero temperatures (*30*, *31*). Thus, it remains unclear how representative the cases are at the Moscow Domodedovo airport.

We link observed glaciation events to industrial point sources by modelling aerosol dispersion from point sources using Hybrid Single-Particle Lagrangian Integrated Trajectory (HYSPLIT) version 5 concentration plume model (*32*) (supplementary methods “Analysis of aerosol dispersion from point sources”). We compare simulated aerosol-polluted areas to the areas of cloud perturbations identified in MODIS satellite data, keeping in mind that the heat and water vapour from the pollution sources are dispersed within the same plumes. The aerosol dispersion plumes overlap exceptionally well with the areas of glaciation, snowfall and reduced cloud cover (Figs 4c and 4d). The difference in azimuth angles (the angle relative to the north) between the observed glaciation events and simulated aerosol-polluted areas downwind of industrial sites is less than 20° for 75% of cases (Fig 4d). Moreover, the shapes of simulated aerosol dispersion plumes are very similar to glaciation events and have distinctive heads pointing towards the pollution sources (example in Fig 4c).

We test if drivers other than aerosols could explain the observed glaciation events by looking for glaciation events downwind nuclear power plants. Nuclear power stations are sources of heat and water vapour, similarly to studied aerosol hot spots, but likely emit little to no aerosols serving as INPs. The heat from the studied aerosol hot spots causes buoyancy and vertical motions of air. The buoyancy-driven cooling of air could be linked to more efficient ice formation in mixed-phase clouds (*33*) and the clouds studied here could potentially be mixed-phase clouds already before they are impacted by aerosol pollution sources. Moreover, the emitted water vapour can cause supersaturation and lead to the formation of a condensation cloud. To cover the range of meteorological conditions favourable for glaciation, we chose 11 nuclear power stations close to the aerosol sources where we identified glaciation events in Eastern Europe (Fig 2a) and analysed supercooled clouds over the winters (December, January, February) 2005 to 2014. In agreement with previous observations of anthropogenic snowfall events at natural draft cooling towers (*18*), we observe glaciation downwind nuclear power stations in five cases (four stations) (Fig 2a, S2). Although glaciation events at nuclear power stations are relatively rare, the existence of these events indicates that reasons other than aerosols serving as INPs may also play a role in the observed glaciation events. An alternative explanation could be that buoyant plumes from the nuclear power plants loft nearby aerosols that serve as INPs.

We observe anthropogenic glaciation of supercooled liquid-water clouds more frequently at specific aerosol sources like processing sites of metals and minerals, including cement production (Table 1). In fact, 78 % of identified aerosol sources leading to glaciation events fall under the categories of metals and minerals (Table 1). Aerosols from these sources are known to serve as INPs, as discussed in the next section. At the same time, CCN perturbations occur predominantly at sulphate-emitting aerosol sources (*26*). Cherepovets steel plant is known to frequently lead to anthropogenic CCN perturbations on clouds (*28*, *29*). At the Cherepovets steel plant, CCN-induced perturbations on clouds are eight times more frequent than glaciation events (Figs S12 and S13).

Which anthropogenic aerosols could nucleate ice at the studied air pollution sources?

We identified anthropogenic glaciation events at 67 industrial aerosol sources in North America, Europe and Asia (supplementary methods “Identification of glaciation events;” Table 1; Fig 2a). The 32 metallurgical plants are mining and processing sites of iron, copper, nickel, and alumina, together with the steel industry and machine building (Table 1). Metallic particles have been previously found in elemental, oxide, and sulfate forms in ice residues under both cirrus and mixed-phase cloud conditions (*34*–*36*). Out of 20 processing sites of minerals, 16 are cement plants. The remaining ones are factories producing asphalt, mineral fertilisers and other minerals. Various minerals are known to be effective INPs (*3*, *37*–*39*). The tectosilicates, including certain feldspars and quartz samples, have been shown to have much greater ice-nucleating activities than clay minerals (*40*). Laboratory experiments have also indicated that cement particles act as INPs (*41*). Cement is produced from calcium carbonates and contains other materials such as CaSO4 (gypsum or anhydrite). While calcium carbonates have been shown to have a relatively low ice nucleating activity, similar to that of the clay minerals (*40*), anhydrite has been implicated in the ice nucleating ability of both volcanic and combustion ashes (*42*, *43*). At three glaciation sites, paper and cellulose are produced, while again previous laboratory experiments support that cellulose particles act as INPs (*44*, *45*). In addition, lignin is also used in paper production and has been shown to be an effective ice nucleant (*46*).

Out of 12 hydrocarbon combustion sites identified to lead to glaciation events, 7 are coal-fired power plants and three are oil refineries. In addition, coal is used to produce thermal energy at multiple studied metallurgical and cement plants. It is important to note that oil and coal are not pure hydrocarbons but also contain minerals (*47*). Moreover, particles can be lofted during combustion, producing airborne ashes like coal fly ash. Laboratory experiments suggest that combustion ashes with various compositions and origins are effective INPs at temperatures below -12 °C (*14*, *43*). Moreover, fly ash from a power plant plume was found to serve as INPs by (*20*). The ability of combustion carbonaceous aerosols (soot) to serve as INPs at the temperatures of mixed-phase clouds is debated and recent laboratory experiments suggest that soot particles are not effective INPs (*3*, *11*, *12*).

More work is clearly needed to better understand the ice-nucleating properties of aerosol emitted from a range of industrial sites and processes. This should not be limited to a better understanding of the activity of candidate aerosol types in a pure form, but needs to take into account the chemical and physical environment that the particles are emitted in. For example, studies of ice nucleation by volcanic ashes show that their ice nucleating ability is strongly altered (enhanced or deactivated) by chemistry that occurs with reactive gases in the eruption plume and cloud (*42*, *48*). In addition, in order to assess the relative role of different INP types in these plumes as well as the wider atmosphere, we need to understand the size distribution of the aerosol types that are emitted. We typically characterise the ice nucleating activity of a material on an active site per surface area basis. Then with knowledge of the aerosol surface area, we can use the active site density to predict the INP concentration (as a function of activation temperature). This is important since the threshold temperature at which significant ice nucleation is observed in the atmosphere is strongly dependent on the available surface area and laboratory-derived threshold temperatures should therefore not be used as an indication of the temperature at which glaciation occurs in clouds.

Possible impacts of ice nucleating particles on clouds

Anthropogenic glaciation of supercooled liquid-water clouds downwind of industrial aerosol hot spots influences cloud cover and radiative fluxes. This is evident from the comparison between the properties of glaciation-affected areas downwind of air pollution hot spots and the properties of the nearby unaffected areas with supercooled liquid-water clouds based on MODIS satellite data (supplementary methods “Analysis of MODIS satellite data for selected aerosol sources;” Fig 2, Fig S14). We hand-logged the plume-shaped glaciation events at five aerosol sources: a copper smelter in Rouyn-Noranda, Canada; an oil refinery in Regina, Canada; a metallurgical plant in Cherepovets, Russia; and cement plants in Fokino and Volsk, Russia. At the time of the Terra MODIS overpass, the reflection of solar radiation to space at 0.545 to 0.565 μm is reduced by 13.7% (±0.7%) in the glaciation-affected areas owing to an 8.3% (±0.8%) reduction in cloud cover and an 18.0% (±3.5%) reduction in cloud optical thickness. At the same time, infrared radiance at 10.78 to 11.28 μm is enhanced by 4.2% (±0.2%) in the glaciation-affected areas, compared to nearby unaffected areas. In addition to glaciation-induced changes in the properties of clouds, the glaciation-induced snow on the ground could also influence radiative fluxes.

The anthropogenic glaciation events identified in this study could be the observable symptoms of the impact of anthropogenic INPs on clouds, in the same way as ship and pollution tracks in liquid clouds reveal the ability of anthropogenic aerosols serving as CCN to perturb liquid clouds (*26*). There is considerable monthly variability in the occurrence of glaciation events, with more cases in cold halfyear (Fig S12). Based on the visual signatures of glaciation events identified in Terra MODIS satellite images, we estimate that the probability of occurrence of glaciation events when susceptible supercooled liquid-water cloud decks occur ranges from 3.3% to 21.1% in cold half-year, with a high sensitivity to the screening of favourable conditions and studied pollution source (Fig 2c; supplementary methods “Meteorological conditions favourable for glaciation events;” Figs S15 and S16). It is also important to consider that visible anthropogenic cloud perturbations occur only at a subset of meteorological conditions and a plume might not be an analogue for a diffuse aerosol distribution, which then introduces sampling biases (*49*).

Further research is needed to understand glaciation events downwind industrial aerosol hot spots. Rare glaciation events downwind of nuclear power plants suggest that factors other than INPs may play a role in the glaciation events. Alternatively, buoyant plumes at nuclear power plants may loft nearby INPs. Moreover, further research is needed to quantify the ability of anthropogenic aerosols to serve as INPs, to quantify their impact on clouds, and to clarify if anthropogenic INPs influence Earth's climate.

References and Notes

1. P. Forster, T. Storelvmo, K. Armour, W. Collins, J.-L. Dufresne, D. Frame, D.J. Lunt, T. Mauritsen, M.D. Palmer, M. Watanabe, M. Wild, H. Zhang, 2021: The Earth's Energy Budget, Climate Feedbacks, and Climate Sensitivity. In *Climate Change 2021 – The Physical Science Basis: Working Group I Contribution to the Sixth Assessment Report of the Intergovernmental Panel on Climate Change* (Cambridge University Press, ed. 1, 2023; https://www.cambridge.org/core/product/identifier/9781009157896/type/book).
2. N. Bellouin, J. Quaas, E. Gryspeerdt, S. Kinne, P. Stier, D. Watson-Parris, O. Boucher, K. S. Carslaw, M. Christensen, A. -L. Daniau, J. -L. Dufresne, G. Feingold, S. Fiedler, P. Forster, A. Gettelman, J. M. Haywood, U. Lohmann, F. Malavelle, T. Mauritsen, D. T. McCoy, G. Myhre, J. Mülmenstädt, D. Neubauer, A. Possner, M. Rugenstein, Y. Sato, M. Schulz, S. E. Schwartz, O. Sourdeval, T. Storelvmo, V. Toll, D. Winker, B. Stevens, Bounding global aerosol radiative forcing of climate change. *Reviews of Geophysics* **58**(1), e2019RG000660 (2020).
3. B. J. Murray, D. O'Sullivan, J. D. Atkinson, M. E. Webb, Ice nucleation by particles immersed in supercooled cloud droplets. *Chem. Soc. Rev.* **41**, 6519 (2012).
4. P. J. DeMott, A. J. Prenni, X. Liu, S. M. Kreidenweis, M. D. Petters, C. H. Twohy, M. S. Richardson, T. Eidhammer, D. C. Rogers, Predicting global atmospheric ice nuclei distributions and their impacts on climate. *Proc. Natl. Acad. Sci. U.S.A.* **107**, 11217–11222 (2010).
5. S. M. Burrows, C. S. McCluskey, G. Cornwell, I. Steinke, K. Zhang, B. Zhao, M. Zawadowicz, A. Raman, G. Kulkarni, S. China, A. Zelenyuk, P. J. DeMott, Ice-nucleating particles that impact clouds and climate: Observational and modeling research needs. *Reviews of Geophysics* **60**(2), e2021RG000745 (2022).
6. U. Lohmann, A glaciation indirect aerosol effect caused by soot aerosols. *Geophys. Res. Lett.* **29**, 1052 (2002).
7. T. Storelvmo, J. E. Kristjánsson, U. Lohmann, Aerosol Influence on Mixed-Phase Clouds in CAM-Oslo. *J. Atmos. Sci.* **65**, 3214–3230 (2008).
8. A. Gettelman, X. Liu, D. Barahona, U. Lohmann, C. Chen, Climate impacts of ice nucleation, *Journal of Geophysical Research: Atmospheres*. **117** (2012).
9. M. P. Adams, M. D. Tarn, A. Sanchez-Marroquin, G. C. E. Porter, D. O’Sullivan, A. D. Harrison, Z. Cui, J. Vergara-Temprado, F. Carotenuto, M. A. Holden, M. I. Daily, T. F. Whale, S. N. F. Sikora, I. T. Burke, J. -U. Shim, J. B. McQuaid, B. J. Murray, A major combustion aerosol event had a negligible impact on the atmospheric ice-nucleating particle population. *JGR Atmospheres*. **125**(22), e2020JD032938 (2020).

10. Z. A. Kanji, A. Welti, J. C. Corbin, A. A. Mensah, Black carbon particles do not matter for immersion mode ice nucleation. *Geophysical Research Letters*. **47**(11), e2019GL086764 (2020).
11. J. Vergara-Temprado, M. A. Holden, T. R. Orton, D. O'Sullivan, N. S. Umo, J. Browse, C. Reddington, M. T. Baeza-Romero, J. M. Jones, A. Lea-Langton, A. Williams, K. S. Carslaw, B. J. Murray, Is Black Carbon an Unimportant Ice-Nucleating Particle in Mixed-Phase Clouds? *JGR Atmospheres*. **123**, 4273–4283 (2018).
12. F. Mahrt, C. Marcolli, R. O. David, P. Grönquist, E. J. Barthazy Meier, U. Lohmann, Z. A. Kanji, Ice nucleation abilities of soot particles determined with the Horizontal Ice Nucleation Chamber. *Atmos. Chem. Phys.* **18**, 13363–13392 (2018).
13. J. Chen, Z. Wu, S. Augustin-Bauditz, S. Grawe, M. Hartmann, X. Pei, Z. Liu, D. Ji, H. Wex, Ice-nucleating particle concentrations unaffected by urban air pollution in Beijing, China. *Atmos. Chem. Phys.* **18**, 3523–3539 (2018).
14. N. S. Umo, B. J. Murray, M. T. Baeza-Romero, J. M. Jones, A. R. Lea-Langton, T. L. Malkin, D. O'Sullivan, L. Neve, J. M. C. Plane, A. Williams, Ice nucleation by combustion ash particles at conditions relevant to mixed-phase clouds. *Atmos. Chem. Phys.* **15**, 5195–5210 (2015).
15. K. Bi, G. R. McMeeking, D. P. Ding, E. J. T. Levin, P. J. DeMott, D. L. Zhao, F. Wang, Q. Liu, P. Tian, X. C. Ma, Y. B. Chen, M. Y. Huang, H. L. Zhang, T. D. Gordon, P. Chen, Measurements of Ice Nucleating Particles in Beijing, China. *JGR Atmospheres*. **124**, 8065–8075 (2019).
16. M. Hartmann, T. Blunier, S. O. Brügger, J. Schmale, M. Schwikowski, A. Vogel, H. Wex, F. Stratmann, Variation of Ice Nucleating Particles in the European Arctic Over the Last Centuries. *Geophysical Research Letters*. **46**, 4007–4016 (2019).
17. C. R. Wood, R. G. Harrison, Anthropogenic snowfall events in the UK: examples of urban weather modification? *Weather*. **64**, 277–280 (2009).
18. M. L. Kramer, D. E. Seymour, M. E. Smith, R. W. Reeves, T. T. Frankenberg, Snowfall Observations from Natural-Draft Cooling Tower Plumes. *Science*. **193**, 1239–1241 (1976).
19. W. M. Culkowski, WEATHER NOTE: AN ANOMALOUS SNOW AT OAK RIDGE, TENNESSEE. *Mon. Wea. Rev.* **90**, 194–196 (1962).
20. F. P. Parungo, P. A. Allee, H. K. Weickmann, Snowfall induced by a power plant plume. *Geophysical Research Letters*. **5**, 515–517 (1978).
21. E. M. Agee, An Artificially Induced Local Snowfall. *Bull. Amer. Meteor. Soc.* **52**, 557–560 (1971).
22. B. Campistron, Interaction between a natural snowfall and a cooling tower plume: An experimental study with a millimetric Doppler radar. *Atmospheric Environment (1967)*. **21**, 1375–1383 (1967).
23. T. Storelvmo, I. Tan, The Wegener-Bergeron-Findeisen process – Its discovery and vital importance for weather and climate, *Meteorologische Zeitschrift*. **24**, 455–461 (2015).
24. S. Platnick, M. D. King, K.G. Meyer, G. Wind, N. Amarasinghe, B. Marchant, G. T. Arnold, Z. Zhang, P. A. Hubanks, B. Ridgway, J. Riedi, MODIS cloud optical properties: User guide for the Collection 6 Level-2 MOD06/MYD06 product and associated Level-3 Datasets. Version 1, 145 (2015).

25. V. Toll, M. Christensen, S. Gassó, N. Bellouin, Volcano and Ship Tracks Indicate Excessive Aerosol-Induced Cloud Water Increases in a Climate Model. *Geophysical Research Letters*. **44** (2017), doi:10.1002/2017GL075280.
26. V. Toll, M. Christensen, J. Quaas, N. Bellouin, Weak average liquid-cloud-water response to anthropogenic aerosols. *Nature*. **572**, 51–55 (2019).
27. J. Rahu, H. Trofimov, P. Post, V. Toll, Diurnal evolution of cloud water responses to aerosols. *JGR Atmospheres*. **127**(10), e2021JD035091 (2022).
28. H. Trofimov, P. Post, E. Gryspeerdt, V. Toll, Meteorological conditions favorable for strong anthropogenic aerosol impacts on clouds. *JGR Atmospheres,* **127**(4), e2021JD035871 (2022).
29. V. Toll, J. Rahu, Strong Anthropogenic Cloud Perturbations Can Persist for Multiple Days. *JGR Atmospheres*, **128**(9), e2022JD038146 (2023).
30. A. J. Heymsfield, G. Thompson, H. Morrison, A. Bansemer, R. M. Rasmussen, P. Minnis, Z. Wang, D. Zhang, Formation and Spread of Aircraft-Induced Holes in Clouds. *Science*. **333**, 77–81 (2011).
31. A. J. Heymsfield, P. C. Kennedy, S. Massie, C. Schmitt, Z. Wang, S. Haimov, A. Rangno, Aircraft-Induced Hole Punch and Canal Clouds: Inadvertent Cloud Seeding. *Bull. Amer. Meteor. Soc.* **91**, 753–766 (2010).
32. R. R. Draxler, G. D. Hess, An overview of the HYSPLIT_4 modelling system for trajectories. *Australian meteorological magazine*, **47**(4), 295-308 (1998).
33. J. Bühl, P. Seifert, R. Engelmann, A. Ansmann, Impact of vertical air motions on ice formation rate in mixed-phase cloud layers. *npj Clim Atmos Sci*. **2**, 36 (2019).
34. D. J. Cziczo, K. D. Froyd, C. Hoose, E. J. Jensen, M. Diao, M. A. Zondlo, J. B. Smith, C. H. Twohy, D. M. Murphy, Clarifying the Dominant Sources and Mechanisms of Cirrus Cloud Formation. *Science*. **340**, 1320–1324 (2013).
35. D. J. Cziczo, O. Stetzer, A. Worringen, M. Ebert, S. Weinbruch, M. Kamphus, S. J. Gallavardin, J. Curtius, S. Borrmann, K. D. Froyd, S. Mertes, O. Möhler, U. Lohmann, Inadvertent climate modification due to anthropogenic lead. *Nature Geosci*. **2**, 333–336 (2009).
36. M. S. Richardson, P. J. DeMott, S. M. Kreidenweis, D. J. Cziczo, E. J. Dunlea, J. L. Jimenez, D. S. Thomson, L. L. Ashbaugh, R. D. Borys, D. L. Westphal, G. S. Casuccio, T. L. Lersch, Measurements of heterogeneous ice nuclei in the western United States in springtime and their relation to aerosol characteristics. *J. Geophys. Res.* **112**, D02209 (2007).
37. Z. A. Kanji, L. A. Ladino, H. Wex, Y. Boose, M. Burkert-Kohn, D. J. Cziczo, M. Krämer, Overview of ice nucleating particles. *Meteorological Monographs*. **58**, 1-1 (2017).
38. A. D. Harrison, T. F. Whale, M. A. Carpenter, M. A. Holden, L. Neve, D. O'Sullivan, J. Vergara Temprado, B. J. Murray, Not all feldspars are equal: a survey of ice nucleating properties across the feldspar group of minerals. *Atmos. Chem. Phys.* **16**, 10927–10940 (2016).
39. A. D. Harrison, K. Lever, A. Sanchez-Marroquin, M. A. Holden, T. F. Whale, M. D. Tarn, J. B. McQuaid, B. J. Murray, The ice-nucleating ability of quartz immersed in water and its

atmospheric importance compared to K-feldspar. *Atmos. Chem. Phys.* **19**, 11343–11361 (2019).

40. J. D. Atkinson, B. J. Murray, M. T. Woodhouse, T. F. Whale, K. J. Baustian, K. S. Carslaw, S. Dobbie, D. O'Sullivan, T. L. Malkin, The importance of feldspar for ice nucleation by mineral dust in mixed-phase clouds. *Nature*. **498**, 355–358 (2013).
41. A. S. R. Murty, Bh. V. R. Murty, Ice nucleation by ordinary Portland cement. *Tellus*. **24**, 581–585 (1972).
42. E. C. Maters, C. Cimarelli, A. S. Casas, D. B. Dingwell, B. J. Murray, Volcanic ash ice-nucleating activity can be enhanced or depressed by ash-gas interaction in the eruption plume. *Earth and Planetary Science Letters*. **551**, 116587 (2020).
43. S. Grawe, S. Augustin-Bauditz, H.-C. Clemen, M. Ebert, S. Eriksen Hammer, J. Lubitz, N. Reicher, Y. Rudich, J. Schneider, R. Staacke, F. Stratmann, A. Welti, H. Wex, Coal fly ash: linking immersion freezing behavior and physicochemical particle properties. *Atmos. Chem. Phys.* **18**, 13903–13923 (2018).
44. N. Hiranuma, O. Möhler, K. Yamashita, T. Tajiri, A. Saito, A. Kiselev, N. Hoffmann, C. Hoose, E. Jantsch, T. Koop, M. Murakami, Ice nucleation by cellulose and its potential contribution to ice formation in clouds. *Nature Geosci*. **8**, 273–277 (2015).
45. N. Hiranuma, K. Adachi, D. M. Bell, F. Belosi, H. Beydoun, B. Bhaduri, H. Bingemer, C. Budke, H.-C. Clemen, F. Conen, K. M. Cory, J. Curtius, P. J. DeMott, O. Eppers, S. Grawe, S. Hartmann, N. Hoffmann, K. Höhler, E. Jantsch, A. Kiselev, T. Koop, G. Kulkarni, A. Mayer, M. Murakami, B. J. Murray, A. Nicosia, M. D. Petters, M. Piazza, M. Polen, N. Reicher, Y. Rudich, A. Saito, G. Santachiara, T. Schiebel, G. P. Schill, J. Schneider, L. Segev, E. Stopelli, R. C. Sullivan, K. Suski, M. Szakáll, T. Tajiri, H. Taylor, Y. Tobo, R. Ullrich, D. Weber, H. Wex, T. F. Whale, C. L. Whiteside, K. Yamashita, A. Zelenyuk, O. Möhler, A comprehensive characterisation of ice nucleation by three different types of cellulose particles immersed in water. *Atmos. Chem. Phys.* **19**, 4823–4849 (2019).
46. S. Bogler, N. Borduas-Dedekind, Lignin's ability to nucleate ice via immersion freezing and its stability towards physicochemical treatments and atmospheric processing. *Atmos. Chem. Phys.* **20**, 14509–14522 (2020).
47. Y. Mamane, J. L. Miller, T. G. Dzubay, Characterization of individual fly ash particles emitted from coal- and oil-fired power plants. *Atmospheric Environment (1967)*. **20**, 2125–2135 (1986).
48. W. D. Fahy, E. C. Maters, R. Giese Miranda, M. P. Adams, L. G. Jahn, R. C. Sullivan, B. J. Murray, Volcanic ash ice nucleation activity is variably reduced by aging in water and sulfuric acid: the effects of leaching, dissolution, and precipitation. *Environ. Sci.: Atmos.* **2**, 85–99 (2022).
49. P. Manshausen, D. Watson-Parris, M. W. Christensen, J.-P. Jalkanen, P. Stier, Invisible ship tracks show large cloud sensitivity to aerosol. *Nature*. **610**, 101–106 (2022).
50. V. V. Salomonson, W. Barnes, E. J. Masuoka, "Introduction to MODIS and an Overview of Associated Activities" in *Earth Science Satellite Remote Sensing*, J. J. Qu, W. Gao, M. Kafatos, R. E. Murphy, V. V. Salomonson, Eds. (Springer Berlin Heidelberg, Berlin, Heidelberg, 2006; http://link.springer.com/10.1007/978-3-540-37293-6_2), pp. 12–32.

51. T. J. Schmit, P. Griffith, M. M. Gunshor, J. M. Daniels, S. J. Goodman, W. J. Lebair, A Closer Look at the ABI on the GOES-R Series. *Bulletin of the American Meteorological Society*. **98**, 681–698 (2017).

52. I. M. Lensky, D. Rosenfeld, Clouds-Aerosols-Precipitation Satellite Analysis Tool (CAPSAT). *Atmos. Chem. Phys.* **8**, 6739–6753 (2008).

53. C. B. Elsenheimer, C. M. Gravelle, Introducing Lightning Threat Messaging Using the GOES-16 Day Cloud Phase Distinction RGB Composite. *Weather and Forecasting*. **34**, 1587–1600 (2019).

54. J. Reid, D. Hudak, S. Boodoo, N. Donaldson, P. Joe, D. Kiktev, A. Melnichuk, Dual-polarisation radar particle classification results during the Sochi Olympic Games. In Eighth European Conf. on Radar in Meteorology and Hydrology, Garmisch-Partenkirchen, Germany, DWD–DLR. [Available online at www. pa. op. dlr. de/erad2014/programme/ExtendedAbstracts/151_Reid. pdf.].

55. H. S. Park, A. V. Ryzhkov, D. S. Zrnić, K.-E. Kim, The Hydrometeor Classification Algorithm for the Polarimetric WSR-88D: Description and Application to an MCS. *Weather and Forecasting*. **24**, 730–748 (2009).

56. H. Hersbach, B. Bell, P. Berrisford, S. Hirahara, A. Horányi, J. Muñoz-Sabater, J. Nicolas, C. Peubey, R. Radu, D. Schepers, A. Simmons, C. Soci, S. Abdalla, X. Abellan, G. Balsamo, P. Bechtold, G. Biavati, J. Bidlot, M. Bonavita, G. De Chiara, P. Dahlgren, D. Dee, M. Diamantakis, R. Dragani, J. Flemming, R. Forbes, M. Fuentes, A. Geer, L. Haimberger, S. Healy, R. J. Hogan, E. Hólm, M. Janisková, S. Keeley, P. Laloyaux, P. Lopez, C. Lupu, G. Radnoti, P. De Rosnay, I. Rozum, F. Vamborg, S. Villaume, J. Thépaut, The ERA5 global reanalysis. *Quart J Royal Meteoro Soc*. **146**, 1999–2049 (2020).

Acknowledgments: We thank Robert Oscar David for the discussions on the ability of various types of anthropogenic aerosols to serve as ice-nucleating particles. We thank Dmitry Moiseev for pointing out previous research on anthropogenic snowfall events.

Funding:

Estonian Research Council grant PRG1726 (VT, JR, HK, HT, PP)

European Research Council (ERC) H2020 project RECAP with grant agreement 724602 (PS)

FORCeS project under the European Union's Horizon 2020 research program with grant agreement 821205 (PS, TS)

Atmospheric System Research (ASR) program of DOE BER under Pacific Northwest National Laboratory (PNNL) project 57131; PNNL is operated for DOE by the Battelle Memorial Institute under contract DE-A06-76RLO 1830 (MC)

GreenFeedBack Hop On project under the European Union's Horizon 2020 research program with grant agreement 101056921 (HJ, VT)

ACCC Flagship funded by the Academy of Finland grant number 337549 (MK)

Natural Environment Research Council (NERC) project NE/T00648X/1 (M-Phase) (BM)

European Union’s Horizon 2020 research and innovation programme under Marie Skłodowska-Curie grant agreement No 860100 (iMIRACLI) (PM)

Author contributions: VT discovered the glaciation events and conceptualised and led the research. HK, HT, JR and VT analysed MODIS satellite observations. JR, PP and VT analysed GOES ABI satellite observations. JR, TV, EH, ND, DM and VT analysed precipitation radar data. PM and MC simulated aerosol dispersion. HK analysed meteorological reanalysis data. HK, JR and VT compiled figures. VT wrote the paper with contributions from all co-authors.

Competing interests: Authors declare that they have no competing interests.

Data and materials availability: We acknowledge the use of imagery from NASA's Worldview application (https://worldview.earthdata.nasa.gov), part of NASA's Earth Observing System Data and Information System (EOSDIS). MODIS data are freely available from https://ladsweb.modaps.eosdis.nasa.gov/search/. NOAA Geostationary Operational Environmental Satellites (GOES) ABI data was accessed from https://registry.opendata.aws/noaa-goes. ERA5 data are freely available from https://cds.climate.copernicus.eu/. The data and software used to analyse glaciation events will be available at https://datadoi.ee/handle/33/610 at the time of the publication and are available at Gitlab for now https://gitlab.cs.ut.ee/ut-climate-research-centre/ACI/glaciation-tracks-published.

Supplementary Materials

Materials and Methods

Figs. S1 to S16

References (*50*–*56*)

Movies S1 to S3

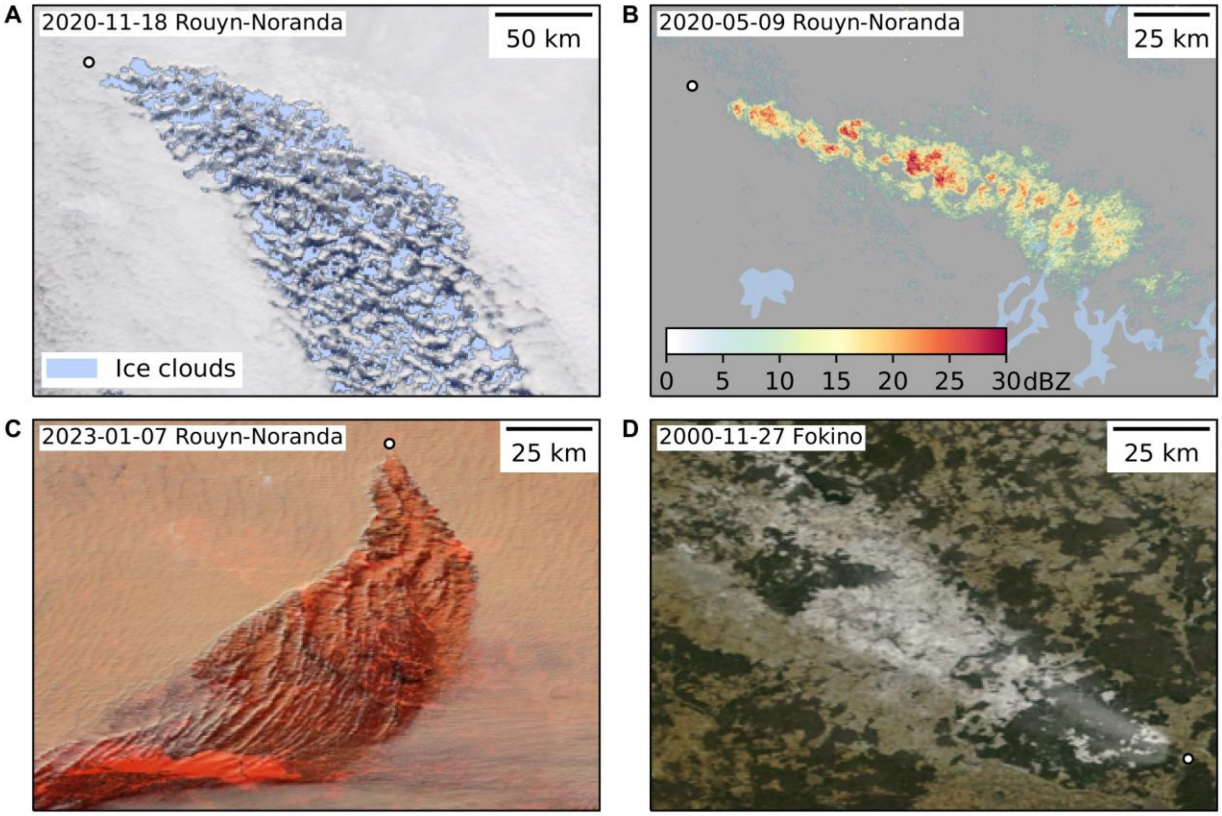

Fig. 1. Plume-shaped areas of anthropogenic glaciation of supercooled clouds, snowfall, reduced cloud cover and snow on the ground for different glaciation events. Remote sensing data reveals ice clouds in the middle of supercooled liquid clouds, snowfall and reduced cloud cover downwind of industrial air pollution hot spots. In all panels, the circle denotes the location of an air pollution source. (**A**) Glaciated area with ice clouds in the middle of supercooled liquid-water clouds downwind of the Copper smelter in Rouyn-Noranda, Canada, overlain on the MODIS daytime true colour satellite image on November 18th 2020. A plume of ice clouds, based on the MODIS cloud phase optical properties product, is highlighted in light blue colour and supercooled liquid clouds are depicted in grey-white colours, based on the true colour satellite image. (**B**) A plume of snow in ground-based precipitation radar reflectivity [dBZ] is shown in green-yellow-red colours downwind of the Copper smelter in Rouyn-Noranda, Canada on May 9th 2020. The ground-based radar is situated in Landrienne, i.e. 85 km northeast of the smelter. (**C**) Area of reduced cloud cover downwind of the Copper smelter in Rouyn-Noranda, Canada, in the MODIS daytime near-infrared composite satellite image on January 7th 2023. The supercooled liquid clouds are depicted in light brownish colours and the plume-shaped area of reduced cloud cover is depicted in darker brownish-red colours as ice and snow cover the ground. In addition, glaciated clouds are shown in red colours. (**D**) A plume-shaped area of snow on the ground downwind of the cement plant in Fokino, Russia, in the MODIS daytime true colour satellite image on November 27th 2000. Snow is depicted in grey-white colours and the ground in green colours. The plume-shaped area of snow on the ground became visible after the glaciation event when the cloud deck cleared away.

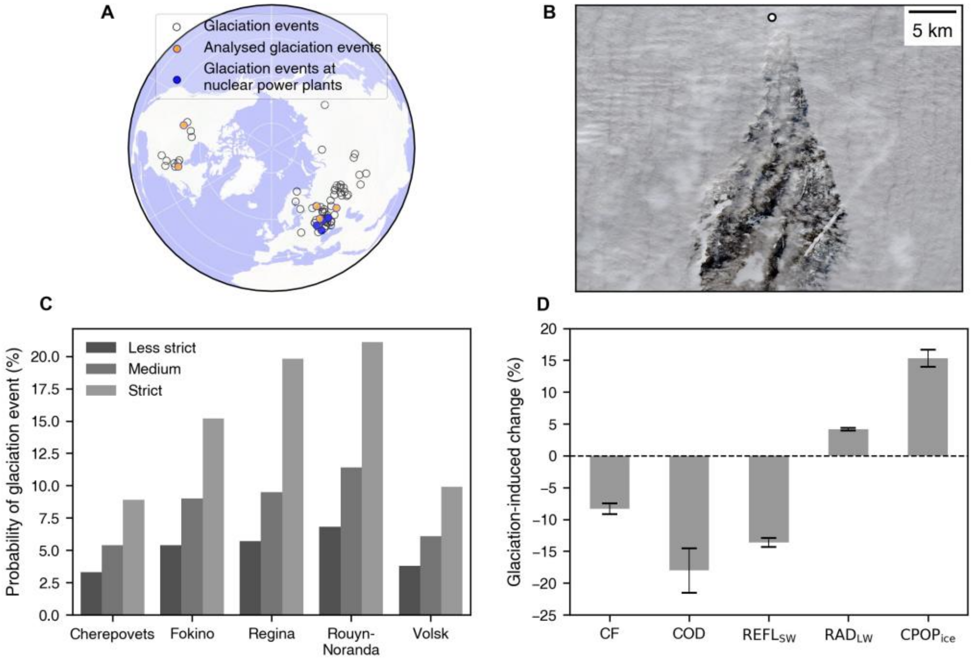

Fig. 2. Anthropogenic glaciation of supercooled liquid-water clouds impacts cloud properties and radiative fluxes. (**A**) Empty circles and orange dots mark the locations of anthropogenic aerosol hot spots where glaciation events have been identified. MODIS data in the years 2000 to 2021 is sampled for the locations given with the orange dots. Glaciation is also observed at nuclear power plants marked with blue dots. (**B**) In the true colour Sentinel-2 MultiSpectral Instrument daytime satellite image, the land surface is seen through the glaciation-induced hole in the supercooled liquid-water cloud deck downwind of the copper smelter in Rouyn-Noranda, Canada on January 9th 2021. The glaciation-affected area is darker compared to the nearby area covered by supercooled liquid-water clouds (depicted in grey-white colours) due to reduced back-scattering of solar radiation to space. The white circle denotes the location of the aerosol source. (**C**) Probability to identify glaciation event in Terra MODIS satellite image in cold half-year (October to March) in case supercooled liquid-water cloud decks susceptible to glaciation occur. The studied sites are a steel plant in Cherepovets, cement plants in Fokino and Volsk, an oil refinery in Regina and a copper smelter in Rouyn-Noranda. The probability depends on the strictness of the screening of favourable conditions (supplementary methods "Meteorological conditions favourable for glaciation events") as indicated by the hue. (**D**) Average fractional changes in cloud fraction (CF), cloud optical depth (COD), shortwave reflectance at 0.545 to 0.565 µm ($REFL_{SW}$), and longwave radiance at 10.78 to 11.28 µm (RAD_{LW}), and the average difference in the fraction of ice-phase pixels in the glaciation-affected areas based on Cloud Phase determined by the Optical Properties algorithm ($CPOP_{ice}$; *24*), compared to nearby unaffected areas based on MODIS data for 298 glaciation events, together with standard errors.

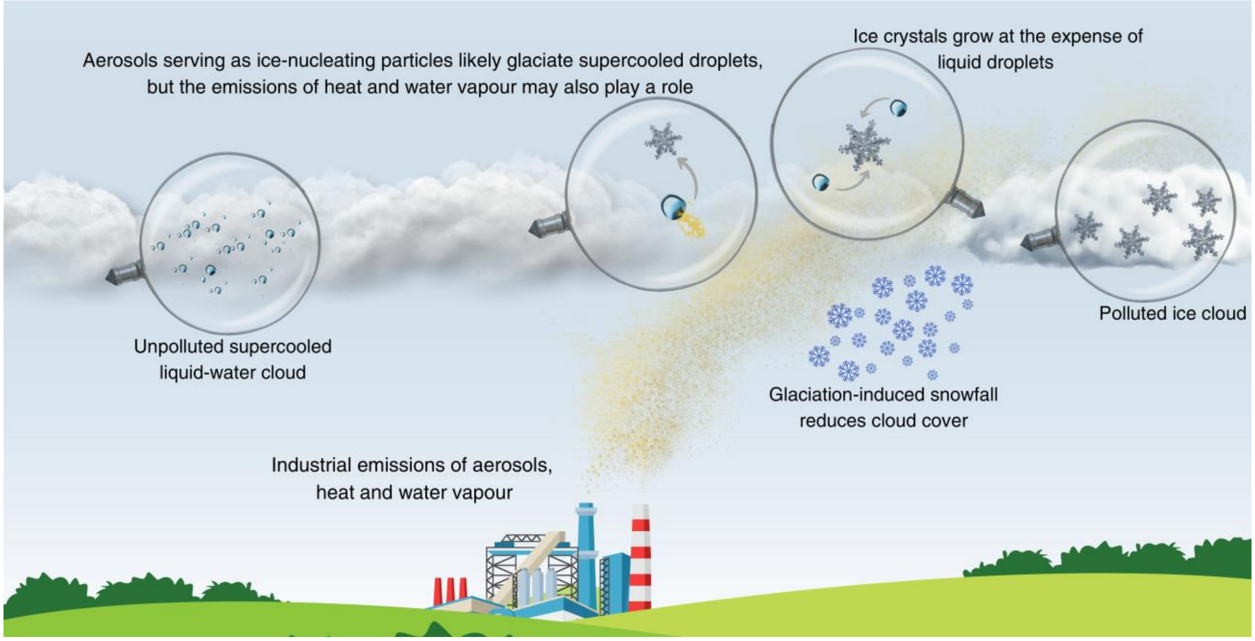

Fig. 3. Industrial emissions lead to the glaciation of supercooled clouds, snowfall and reduced cloud cover, while aerosols serving as ice-nucleating particles likely play a dominant role in the glaciation. Ice clouds in the middle of supercooled liquid-water clouds and snowfall are observed downwind of industries like metallurgical and cement factories. Anthropogenic aerosols serving as INPs likely transform supercooled cloud droplets into ice crystals at the studied air pollution hot spots, although the emissions of heat and water vapour may also play a role, as suggested by glaciation events downwind nuclear power plants. The ice crystals could subsequently grow at the expense of supercooled droplets. Finally, the growth of ice crystals leads to snowfall that reduces cloud cover.

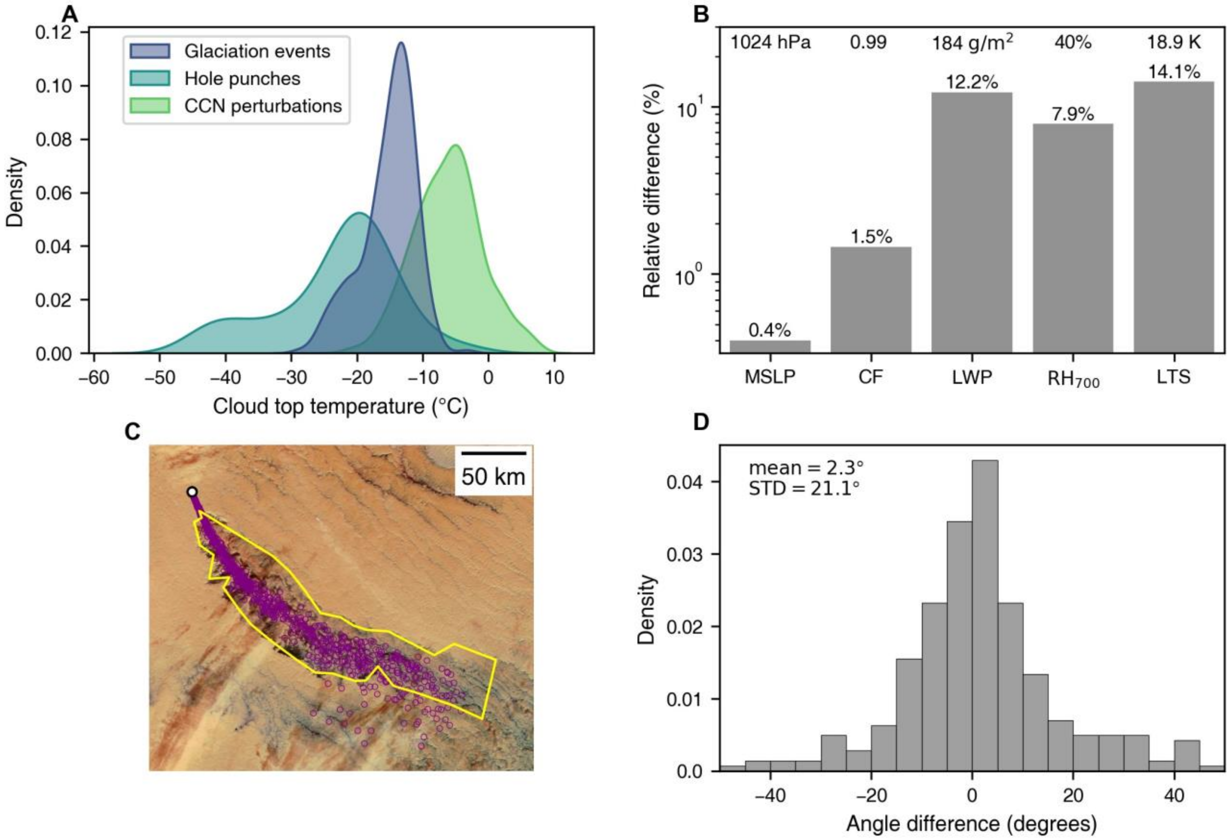

Fig. 4. Linking glaciation events to industrial emissions. (**A**) MODIS cloud top temperatures (°C). Glaciation events downwind aerosol hot spots occur at colder temperatures compared to cloud condensation nuclei (CCN) perturbations but at higher subzero temperatures compared to aircraft-induced hole punch clouds at Moscow Domodedovo airport. The temperatures for the Volsk cement plant in Russia are not shown, as we only identified glaciation events there. (**B**) The relative difference [%] of meteorological conditions characteristic of glaciation events from conditions characteristic of CCN perturbations. Average mean sea level pressure (MSLP), cloud fraction (CF), liquid water path (LWP), relative humidity at 700 hPa pressure level (RH700) and lower tropospheric stability (LTS) are compared. On the top of the panel, average conditions for glaciation events are given. The data for the Volsk cement plant in Russia are not shown, as we only identified glaciation events there. (**C**) MODIS daytime near-infrared composite satellite image of supercooled liquid-water clouds on November 18th 2006. The supercooled clouds are depicted in brownish colours. The yellow polygon surrounds the area of a glaciation event identified and hand-logged in satellite data. The glaciated area overlaps with the simulated aerosol-polluted area, given with violet dots, strikingly well. The white circle denotes the location of the aerosol source - the copper smelter in Rouyn-Noranda, Canada. (**D**) The differences in azimuths (degrees) between glaciation events identified in MODIS satellite data and simulated aerosol-polluted areas downwind of industrial aerosol sources are relatively small. The differences that are larger than 50 degrees are not shown.

Table 1. Emissions from metallurgy, processing of minerals, hydrocarbon combustion, paper production, and nuclear power plants lead to the glaciation of supercooled liquid-water clouds. For each emission source group, the count of identified emission sources leading to glaciation is given together with the list of identified emission source types.

Emission source group	**List of emission sources**	**Count of identified emission sources leading to glaciation events**
Metallurgy	Machine building, processing of steel, iron, copper, nickel, alumina	32
Minerals	Production of cement, asphalt, and mineral fertilisers	20
Hydrocarbon combustion	Coal-fired power plants, oil refineries, production of petrochemicals	12
Cellulose	Production of cellulose and paper	3
Low aerosol emission power plants	Nuclear power plants	4

Supplementary Materials for

Glaciation of liquid clouds, snowfall and reduced cloud cover at industrial aerosol hot spots

Velle Toll, Jorma Rahu, Hannes Keernik, Heido Trofimov, Tanel Voormansik, Peter Manshausen, Emma Hung, Daniel Michelson, Matthew W. Christensen, Piia Post, Heikki Junninen, Benjamin J. Murray, Ulrike Lohmann, Duncan Watson-Parris, Philip Stier, Norman Donaldson, Trude Storelvmo, Markku Kulmala, Nicolas Bellouin

Corresponding author: velle.toll@ut.ee

The PDF file includes:

Materials and Methods
Figs. S1 to S16

Other Supplementary Materials for this manuscript include the following:

Movies S1 to S3

Materials and Methods

Identification of glaciation events

We used the US National Aeronautics and Space Administration (NASA) Global Imagery Browse Services (GIBS) near-infrared daily composite Terra MODIS (*50*) satellite images available through the NASA Worldview interactive interface for the visual identification of glaciation events (Fig 1c, S1, S2, Table 1). In this composite, measurements at the wavelengths 0.459–0.479 μm, 1.628–1.652 μm and 2.105–2.155 μm are used with a horizontal resolution of 500 metres. In these composite images, ice clouds can be visually distinguished from liquid-water clouds due to the enhanced absorption in the shortwave infrared bands. Unfortunately, this composite is not available for Aqua MODIS due to the failure of the band six sensors shortly after launch.

Establishing a link between glaciation, snowfall and reduced cloud cover in supercooled liquid-water cloud decks allowed us to identify glaciation events based on plume-shaped areas of reduced cloud cover in Terra MODIS images. Reduced cloud cover served as primary evidence for the visual identification of glaciation events. In some cases, ice clouds in the middle of supercooled liquid-water clouds served as secondary evidence for the visual identification of glaciation events. The glaciation events are identified in case the glaciation-affected cloud area can be confidently linked to the industrial air pollution source. The perturbation area should have a clear head pointing towards the pollution source or the area of the cloud perturbation (area of reduced cloud cover) should be plume-shaped, indicating that the air pollution source is inducing the observed cloud perturbation. The visual signatures of glaciation events have both similarities and differences compared with the ship-track-like anthropogenic CCN perturbations on clouds (27). Although glaciation events and CCN perturbations are both characterised by plume-shaped areas of cloud perturbations, the glaciation events are visually different from ship-track-like strong CCN perturbations on clouds (Fig S6). CCN perturbations are characterised by enhanced near-infrared reflectance due to more numerous and smaller cloud droplets. In the case of CCN perturbations, there is no clear reduction in cloud cover and no clear change in the cloud phase.

The identification of glaciation events in NASA GIBS images using NASA Worldview is sensitive to the used zoom level, i.e. the extent of the geographical area that is checked for cloud perturbations at a particular time. When susceptible clouds or perturbation-like signatures were seen at a specific geographical region while analysing a larger geographical area, then we zoomed into the specific region for more detailed visual inspection. In addition, the manual identification of the cloud perturbations is likely to be sensitive to the ability of human observer to identify contrasts in satellite images by the naked eye. We used auxiliary layers indicating the locations of anthropogenic aerosol point sources. We used locations of metallurgical and cement plants, power plants and oil refineries. In addition, we used satellite images of night lights to indicate hot spots of human activity and a layer of human settlements as locations of possible aerosol sources. After detecting glaciation events in Terra MODIS satellite images, we identified the aerosol sources leading to glaciation using Landsat satellite images and Google Maps.

To clarify the role of factors other than aerosols, we also identified glaciation events in near-infrared composite Terra MODIS satellite images downwind nuclear power plants in Eastern Europe (Fig S2), Latitudes 45° to 59° and Longitudes 25° to 49° in the winter months (December, January, February) in years 2005 to 2014. Winter was chosen as glaciation events most frequently occur in winter (Figs S10 and S11). The region in Eastern Europe was chosen as there are eleven nuclear power stations within this area. Moreover, as in this particular geographical region the glaciation events are seen downwind of industrial aerosol hot spots, we assume that the meteorological conditions favour the occurrence of anthropogenic glaciation events in the area.

Analysis of MODIS satellite data for selected aerosol sources

We sampled the time series of anthropogenic glaciation events for the years 2000 to 2021 for five different aerosol sources. The five sources were a copper smelter in Rouyn-Noranda (Latitude 48.2530°, Longitude -79.0163°), Canada; an oil refinery in Regina (Latitude 50.4849°, Longitude -104.5763°), Canada; steel plant in Cherepovets (Latitude 59.1442°, Longitude 37.8482°), Russia; cement plants in Fokino (Latitude 53.4445°, Longitude 34.4092°) and Volsk (Latitude 52.0517°, Longitude 47.4355°), Russia. These sources were selected to include sites where glaciation events are frequent enough for more detailed analysis, to include emission sources both from Eurasia and North America, and to include various types of pollution sources (copper smelter, oil refinery, steel plant, two cement plants) emitting different types of aerosols. Including a larger number of pollution sources would have been challenging due to the large amount of work needed for the manual sampling of glaciation events. For each day in the years 2000 to 2021 and for each location, we visually checked the Terra MODIS daytime image for the presence of a glaciation event and CCN-induced cloud perturbation. As Terra is a polar orbiter, there was one daytime image per day for each location. Initially, we detected 104 glaciation events for Rouyn-Noranda, 67 events for Regina, 63 events for Cherepovets, 89 events for Fokino and 52 events for Volsk. After the data screening described below, 84 glaciation events for Rouyn-Noranda, 59 events for Regina, 40 events for Cherepovets, 74 events for Fokino and 41 events for Volsk were included in the final analysis of MODIS data presented in Fig 2d and Fig S14. The estimate that at the Cherepovets steel plant CCN-induced perturbations on clouds are eight times more frequent than glaciation events is calculated by dividing the total count of CCN perturbations on clouds (319) by the total count of screened glaciation events (40).

For all the glaciation events, we hand-logged the areas affected by anthropogenic emissions, e.g. the yellow polygon in Fig 4c. We hand-logged the plume-shaped perturbation areas, where the visual contrast due to change in cloud cover or cloud phase was seen in the near-infrared composite MODIS satellite image. A particular case was identified and hand-logged only if it was possible to link the glaciation-affected cloud area to the sampled aerosol point source. It is important to note that it can be subjective to identify how far from the industrial point source a particular perturbation area exactly ends. We have published the images of perturbation areas and the geographical coordinates of hand-logged polygons so that the results can be replicated and extended.

After logging the glaciation-affected polygons, we used an automated algorithm to calculate average properties for the hand-logged glaciation-affected areas and surrounding unaffected areas. First, we selected a 5 km wide buffer area around each hand-logged glaciation-affected area while we excluded the MODIS pixels within this buffer area. Then, we selected 20 kilometres wide unaffected area around each buffer area. We then applied pixel-level data screening for both the glaciation-affected and unaffected areas. Multi-layer clouds and clouds with cloud top pressure less than 500 hPa were screened out from the analysis of cloud properties, shortwave reflectances and longwave radiances. It is important to note that we show the differences in shortwave reflectances and longwave radiances at the time of the Terra MODIS overpass and not over the full diurnal cycle. To exclude possible fog cases, we excluded the cases where the average cloud top height in the unaffected area was less than 250 m; in total, there were six such cases. The average cloud top height in the unaffected areas for the analysed glaciation events is 2891 m. We used MODIS Collection 6.1 1-km-resolution level-2 cloud-property dataset MOD06_L2 from Terra satellite (*24*) to compare the glaciation-affected and unaffected cloud properties (Figs 2d and S14). In addition, we used level-1b calibrated radiances from Terra MODIS. We excluded cases where cloud optical depth, cloud top height, cloud fraction or shortwave reflectance data were unavailable for the unaffected area; there were 22 such cases. In Fig 2d, comparing glaciation-affected areas to nearby unaffected areas, average fractional changes are given for cloud fraction (CF), cloud optical depth (COD), shortwave reflectance at 0.545 to 0.565 µm ($REFL_{SW}$), and longwave radiance at 10.78 to 11.28 µm (RAD_{LW}), and average absolute difference is given for the fraction of ice-phase pixels based on Cloud Phase determined by the Optical Properties algorithm ($CPOP_{ice}$). Standard errors are given for average fractional changes in CF, COD, $REFL_{SW}$, RAD_{LW} and for the average absolute difference in $CPOP_{ice}$. The same parameters are given in Fig S14.

We analysed MOD06_L2 Terra MODIS cloud top temperatures (*24*) for the glaciation events and CCN-induced perturbations at Rouyn-Noranda, Regina, Cherepovets, Fokino and Volsk for the years 2000 to 2021 (Fig 4a, Fig S9a). The data for the Volsk cement plant in Russia are not shown in Fig 4a, as we only identified glaciation events there. In addition, we analysed MOD06_L2 Terra MODIS cloud top temperatures for hole punch clouds near Moscow Domodedovo airport (Latitude 55.408611°, Longitude 37.906111°) for the years 2000 to 2021 (Fig 4a). For each CCN-induced cloud perturbation, each glaciation event and each aircraft-induced hole punch cloud, cloud top temperatures were averaged over a circle with a radius of 10 kilometres. The circle surrounded Moscow Domodedovo airport (Latitude 55.408611°, Longitude 37.906111°) for the hole punch clouds and aerosol point sources for CCN-induced perturbations and glaciation events. For CCN-induced perturbations and glaciation events, pixels with multilayer clouds and clouds with cloud top pressure less than 500 hPa were screened out from the analysis. For hole punch clouds, pixels with multilayer clouds were screened out from the analysis, but as hole punches also occur in higher clouds, cloud top pressure was not used for screening. Fig S8a shows that cloud top pressures are rarely lower than 600 hPa for glaciation events and previous work has shown that this is also true for CCN-induced cloud perturbations (28). The cloud top temperatures for hole punch clouds, glaciation events and CCN-induced perturbations are compared in Fig 4a. For cloud top temperatures of glaciation events, the 5th percentile is -24 °C, and the 95th percentile is -10 °C. For cloud top temperatures of CCN perturbations, the 5th percentile is -15 °C, and the 95th percentile is 2 °C.

Analysis of GOES ABI satellite data

After identifying glaciation events using Terra MODIS data, we analysed the temporal evolution of glaciation events for Rouyn-Noranda and Regina, Canada, using GOES ABI data (*51,* Fig S5, Movies S1 and S2). At the nadir, the GOES ABI data has a horizontal resolution of 0.5 to 2 kilometres, depending on the channel. We visually inspected the GOES ABI 3.9 µm channel measurements and various red-green-blue (RGB) composite images. We used the following RGB composites: night microphysics, natural colour, day microphysics, cloud phase distinction, convection, snow, cloud top, night fog and dust RGBs (*52, 53*). We used the Satpy Python library to create these composites.

GOES ABI data were available for 28 cases at Rouyn-Noranda and 11 cases at Regina. We recorded times when glaciation events first became visible together with the times when glaciation-induced cloud perturbations were no longer visible to analyse for how long the glaciation-induced cloud perturbations were visible. We also recorded the cases where the formation of ice clouds in the middle of a supercooled liquid-phase cloud deck was seen in satellite data and calculated the fraction of cases where ice clouds were visually identified.

Analysis of ground-based precipitation radar data

Data from two operational Canadian weather radar sites were incorporated in this study, at Landrienne, Québec, and Bethune, Saskatchewan (Figs S3 to S5, Movies S2 and S3). Landrianne radar is close to Rouyn-Noranda and allows to study the glaciation events downwind of the copper smelter. Bethune radar is near Regina and allows to study the glaciation events downwind of the oil refinery. Both radars were C-band Doppler horizontal-polarisation radars with 250 kW magnetron transmitters until they were replaced in 2019. Since 2019, they are S-band dual-polarisation radars with 1 MW klystron transmitters. The half-power beamwidths of the old C-band radars were 1.1° at Landrienne and 0.62° at Bethune. Both new S-band radars' half-power beamwidths are 0.9° with 500 meters bin length.

The C-band scan strategy involved acquiring a reflectivity-only (not Doppler processed) volume consisting of 24 sweeps in top-down order with a maximum range of 250 km. Doppler data were then collected as a set of four individual sweeps with maximum ranges of 100 or 120 km. The total acquisition cycle was ten minutes. The new S-band scan strategy acquires a volume comprising 17 sweeps containing ten variables, both conventional and polarimetric, every six minutes; the maximum range of the lowest six sweeps is 240 km. A Canadian operational dual-polarisation-based particle classification product (*54*) is used in this study. It is based on the algorithm developed for the Next Generation Weather Radar (NEXRAD) network in the United States (*55*) and classifies particles into the same ten types as the NEXRAD algorithm. The classification product uses temperature information from a numerical weather prediction model together with the radar data and fuzzy logic to distinguish between solid and liquid phase precipitation classes, along with classes that are non-meteorological.

For Landrienne, radar data were available for 77 glaciation events in the years 2005 to 2021, while dual-polarisation data were available for 14 cases. For Bethune, radar data were available for 45 glaciation events in the years 2005 to 2021, while dual-polarisation data were available for 10 cases. The radar reflectivity data were visually checked for plumes of precipitation downwind of aerosol sources. We identified plumes of precipitation for 16 cases for Landrienne and for 19 cases for Bethune. For each plume of precipitation, we recorded the start time, peak time and end time of precipitation following visual inspection of radar reflectivity images. We then hand-logged the area where precipitation was seen during the peak time to calculate the snowfall rate for each case. Furthermore, we hand-logged the areas of precipitation accumulations from the precipitation start time to the precipitation end time. Then, we calculated the snowfall accumulation for each accumulation area. In the main paper, the average accumulation area 2161 km^2 is given. For the calculation of snowfall rates (S [cm/h]) and accumulations from radar reflectivity (Z [mm^6/m^3]) we used the relationship operationally used in Canada: $Z = 399 * S^{2.21}$. This gives the approximate depth of fresh snow on the ground. The snow water equivalent snowfall rate (S_e [mm/h]) would be in units mm/h using the relationship $Z = 399 * S_e^{2.21}$. Throughout the main paper, we give the approximate snow depths on the ground. The average snowfall rate of 1.2 mm/h is an average of 34 precipitation cases at Rouyn-Noranda and Regina in Canada. It is probably not as representative as average cloud responses to glaciation studied at five sites in North America and Eurasia (Fig 2d).

Analysis of aerosol dispersion from point sources

We simulated the spatial distributions of the emitted aerosol particles for Rouyn-Noranda, Regina, Cherepovets, Fokino and Volsk for the years 2000 to 2021 using the Hybrid Single-Particle Lagrangian Integrated Trajectory (HYSPLIT) version 5 concentration plume model (*32*). The model predicts the concentration of aerosol particles in 60-minute time steps. The model is run in the forward direction for 24 hours prior to the Terra satellite overpass time. During each time step, 2500 particles are released from the industrial aerosol hot spot. The location of the plume is largely dictated by the input meteorological conditions. We use state-of-the-art European Centres for Medium Range Forecasts (ECMWF) ERA5 reanalysis data (*56*). We converted the meteorological data to the Air Resources Laboratory (ARL) format and read it into HYSPLIT. ERA5 is a high-resolution realisation atmospheric data set with a horizontal resolution of 31 km (TL639 spectral grid). The pressure level data are provided for 37 levels in the vertical, with the top level located at 1 hPa, providing hourly estimates of a comprehensive suite of atmospheric, terrestrial, and oceanic climate variables.

We compared the azimuths (angle relative to the north) between HYSPLIT aerosol dispersion plumes and hand-logged glaciation-induced cloud perturbations for Rouyn-Noranda, Regina, Cherepovets, Fokino and Volsk for the years 2000-2021. For the azimuths, we assume the observer is at the aerosol emission source. The comparison is illustrated in Fig 4c and the frequency distribution for the differences in azimuths is shown in Fig 4d. From the final analysis of MODIS data (Fig 2d), we excluded the cases where the difference between the azimuths of aerosol dispersion plumes and hand-logged glaciation-induced cloud perturbations were larger than 90 degrees. Altogether, there were 18 such cases and these were excluded to avoid possible false identifications of glaciation events. In addition, the HYSPLIT simulations were not available for 31 cases for technical reasons, and these cases were left out of the analysis of MODIS data as well (Fig 2d). However, the results are similar irrespective of the data screening of analysed glaciation cases. Without screening (based on HYSPLIT data, MODIS cloud top height less than 250 m, and availability of MODIS cloud optical depth, cloud top height, cloud fraction and shortwave reflectance data for the unaffected area) the industry-affected glaciated clouds backscatter 14% less solar radiation to space, compared to the nearby liquid-water clouds. The reduced backscatter results from a 9% reduction in cloud cover and a 19% reduction in cloud optical thickness.

Meteorological conditions favourable for glaciation events

We compare the meteorological conditions favourable for glaciation events at Rouyn-Noranda, Regina, Cherepovets, and Fokino in the years 2000 to 2021 to the meteorological conditions favourable for CCN-induced cloud perturbations at the same sites (Fig 4b). The data for the Volsk cement plant in Russia are not shown in Fig 4b, as we only identified glaciation events there. To analyse the meteorological conditions, we used both MODIS cloud properties (*24*) and ERA5 atmospheric reanalysis data (*56*). We used MODIS Collection 6.1 1-km-resolution level-2 cloud-property dataset MOD06_L2 from Terra satellite (*24*), similar to the analysis of cloud responses in glaciation-affected areas, compared to the nearby unaffected areas. For ERA5, we used data from 16 UTC for Rouyn-Noranda, from 18 UTC for Regina, and from 9 UTC for Fokino and Cherepovets to align the meteorological conditions to approximate Terra overpass time as Terra MODIS data is used to identify the glaciation events in the first place. Both for MODIS and ERA5 data, we averaged the conditions over a circle with a radius of 10 kilometres. The centre of the circle was at the studied aerosol point sources both for CCN-induced cloud perturbations and glaciation events. In addition to the averages in Fig 4b, we show frequency distributions in Figs S7 and S8.

We show climatological cloud top temperatures for wintertime (December, January, February) supercooled liquid-water cloud decks based on Terra MODIS level 3 data (1-degree horizontal resolution) for days when cloud fraction is equal to or larger than 80%, cloud top pressure is more than 500 hPa, less than 25% of the clouds are ice phase clouds (Cloud_Retrieval_Fraction_Ice), less than 25% of the clouds are multilayer clouds (ML_Fraction_Combined), and the cirrus fraction (Cirrus_Fraction_Infrared) is below 25% for Rouyn-Noranda, Regina, Cherepovets, Fokino and Volsk for the years 2000 to 2021 at the 1-degree horizontal resolution (Fig S9c). We use the nearest gridpoint to each studied pollution source from level 3 daily 1-degree horizontal resolution data throughout the analysis. The same time period, i.e. 2000 to 2021, is considered to account for the meteorological conditions favourable for glaciation events and CCN perturbations on clouds. We assume that a glaciation event is expected when the cloud fraction is larger than 80%, cloud top pressure is more than 500 hPa, less than 25% of the clouds are ice phase clouds (Cloud_Retrieval_Fraction_Ice), less than 25% of the clouds are multilayer clouds (ML_Fraction_Combined), the cirrus fraction (Cirrus_Fraction_Infrared) is below 25%, and cloud top temperatures are between -24 °C and -10 °C in MODIS Terra level 3 daily data at the studied site in Figs S12a and S13b. We assume that a CCN perturbation is expected when the cloud fraction is larger than 80%, cloud top pressure is more than 500 hPa, less than 25% of the clouds are ice phase clouds (Cloud_Retrieval_Fraction_Ice), less than 25% of the clouds are multilayer clouds (ML_Fraction_Combined), the cirrus fraction (Cirrus_Fraction_Infrared) is below 25%, and cloud top temperatures are between -15 °C and 2 °C in MODIS Terra level 3 daily data at the studied site in Figs S12b and S13b.

We selected the thresholds for the screening criteria to identify liquid-water cloud decks favourable for the occurrence of glaciation events and CCN perturbations on clouds based on the conditions characteristic to days with CCN perturbations and glaciation events, respectively (Figs S15 and S16). It is important to note that while we use 1-degree resolution level 3 data to identify days with liquid-water cloud decks favourable for glaciation events and CCN perturbations, we used 1-kilometre resolution level 2 MODIS data to derive screening criteria for cloud top temperatures. In level 3 data, the cloud top temperatures (also cloud top pressure, cloud fraction) are averages over all clouds in the sampled 1 by 1-degree area and allowing for 25% of ice clouds, 25% multilayer clouds and 25% cirrus clouds, means that their properties influence the averages over the 1 by 1-degree grid box. However, we have checked that cloud top temperatures and cloud top pressures from level 3 data for glaciation events and CCN perturbations support choosing the selected thresholds (Figs S15 and S16, S9). Moreover, we have tested that the chosen thresholds for screening criteria work acceptably well. Using the chosen thresholds for criteria based on level 3 data, 74.8% of visually identified glaciation event days and 66.5% of visually identified CCN perturbation days are found to be favourable to glaciation and CCN perturbations, respectively.

We quantified the sensitivity of the probability of identifying a glaciation event in Terra MODIS satellite image when susceptible clouds occur in the cold half-year to the thresholds of screening criteria characterising conditions potentially favouring a glaciation event. In Fig 2c medium category, we assume that glaciation could occur in supercooled liquid-water cloud decks when the cloud fraction is larger than 80%, cloud top pressure is more than 500 hPa, less than 25% of the clouds are ice phase clouds (Cloud_Retrieval_Fraction_Ice), less than 25% of the clouds are multilayer clouds (ML_Fraction_Combined), the cirrus fraction (Cirrus_Fraction_Infrared) is below 25%, and cloud top temperatures are between -24 °C and -10 °C in MODIS Terra level 3 daily data at the studied site. In Fig 2c, the probabilities of identifying a glaciation event in Terra MODIS satellite image when susceptible clouds occur is 5.4% for steel plant in Cherepovets, 9.0% for cement plant in Fokino, 6.1% for cement plant in Volsk, 9.5% for oil refinery in Regina and 11.4% for copper smelter in Rouyn-Noranda, in the cold half-year. Alternatively, we assume that glaciation could occur when the cloud fraction is larger than 80%, cloud top pressure is more than 500 hPa, less than 10% (40%) of the clouds are ice phase clouds (Cloud_Retrieval_Fraction_Ice), less than 10% (40%) of the clouds are multilayer clouds (ML_Fraction_Combined), the cirrus fraction (Cirrus_Fraction_Infrared) is below 10% (40%), and cloud top temperatures are between -24 °C and -10 °C (-27 °C and -7 °C) in MODIS Terra level 3 daily data at the studied sites. With such stricter (less strict) thresholds, we get probabilities of identifying a glaciation event in Terra MODIS satellite image when susceptible clouds occur is 8.9% (3.3%) for steel plant in Cherepovets, 15.2% (5.4%) for cement plant in Fokino, 9.9% (3.8%) for cement plant in Volsk, 19.8% (5.7%) for oil refinery in Regina and 21.1% (6.8%) for copper smelter in Rouyn-Noranda, in the cold half-year. In Fig 2c, these are shown as strict and less strict categories, respectively. With such more (less) strict thresholds for criteria, 57.4% (88.3%) of visually identified glaciation event days are found to be favourable to glaciation based on level 3 data.

Estimating the frequency of occurrence of clouds susceptible to anthropogenic emissions using 1-degree horizontal resolution MODIS level 3 data is a different approach compared to (28), where visual inspection of MODIS Terra near-infrared composite images (in these composite images, measurements at the wavelengths 0.459–0.479 µm, 1.628–1.652 µm and 2.105–2.155 µm are used with a horizontal resolution of 500 metres) was carried out to identify susceptible clouds. Thus, we do not expect our occurrence probabilities of glaciation events and CCN perturbations to be directly comparable to the occurrence probabilities of CCN perturbations on clouds as estimated by (28).

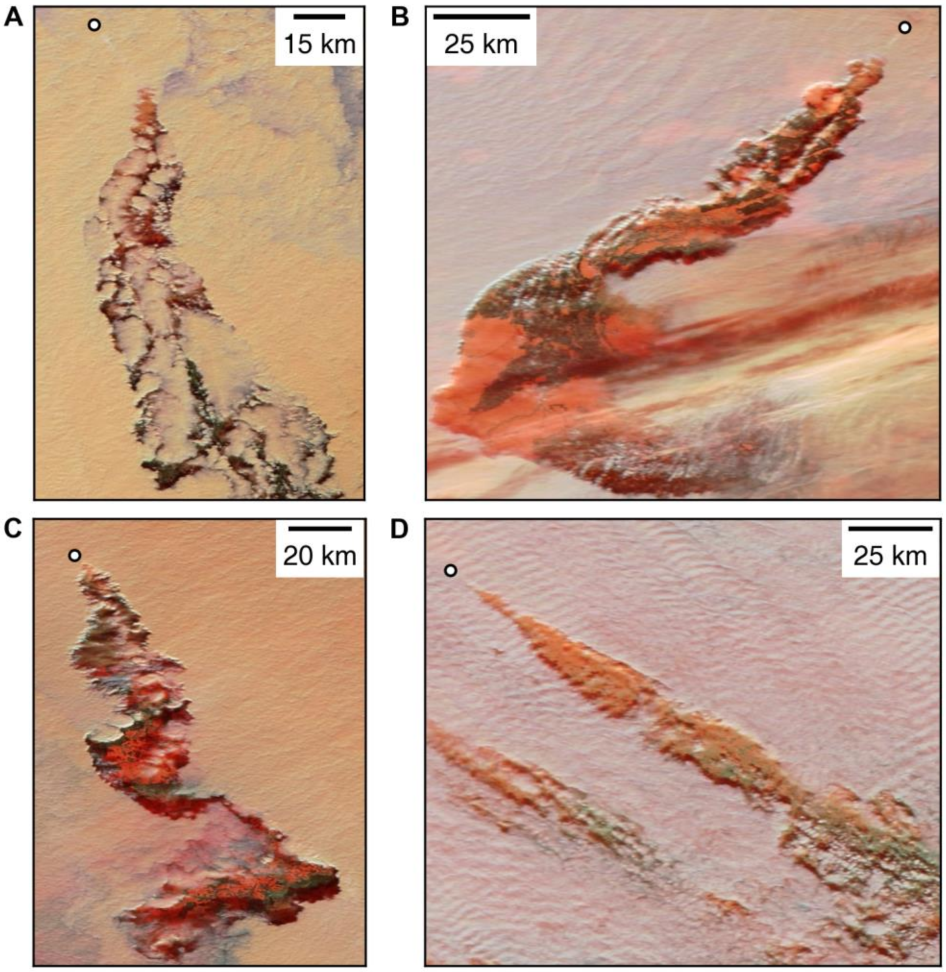

Fig. S1.

Further examples of glaciation events in supercooled cloud decks downwind of industrial air pollution hot spots. Glaciation events in Terra MODIS near-infrared composite images downwind of (**A**) copper smelter in Rouyn-Noranda, Canada on November 20th, 2006, (**B**) metallurgical plant in Flin Flon, Canada on January 15th, 2001, (**C**) cement production in Fokino, Russia on January 6th, 2020, and (**D**) oil refinery in Regina, Canada on December 4th, 2008. The circles mark the locations of anthropogenic aerosol sources.

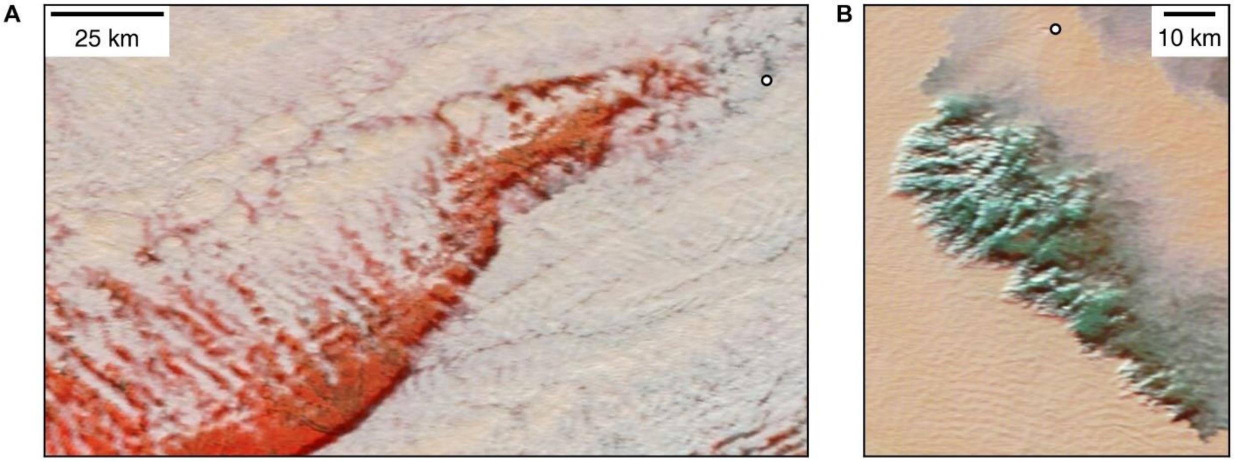

Fig. S2.

We identified five glaciation events downwind nuclear power plants in Eastern Europe. Glaciation events in Terra MODIS near-infrared composite images downwind of (**A**) South Ukraine nuclear power plant in Ukraine on January 11th, 2006, (**B**) Novornezh nuclear power plant in Russia on December 16th, 2008.

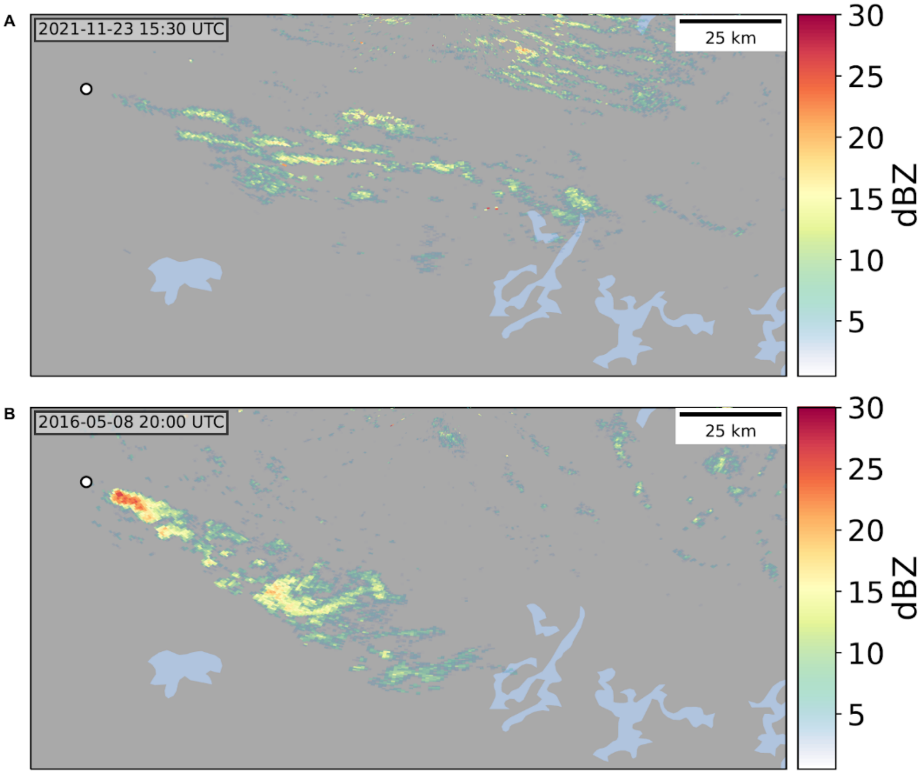

Fig. S3.

Further examples of plume-shaped snowfall areas in ground-based radar data. The glaciation-induced plumes of snow are seen in ground-based precipitation radar reflectivity [dBZ] downwind copper production in Rouyn-Noranda, Canada. Snow plumes on (**A**) November 23rd, 2021, and (**B**) May 8th, 2016.

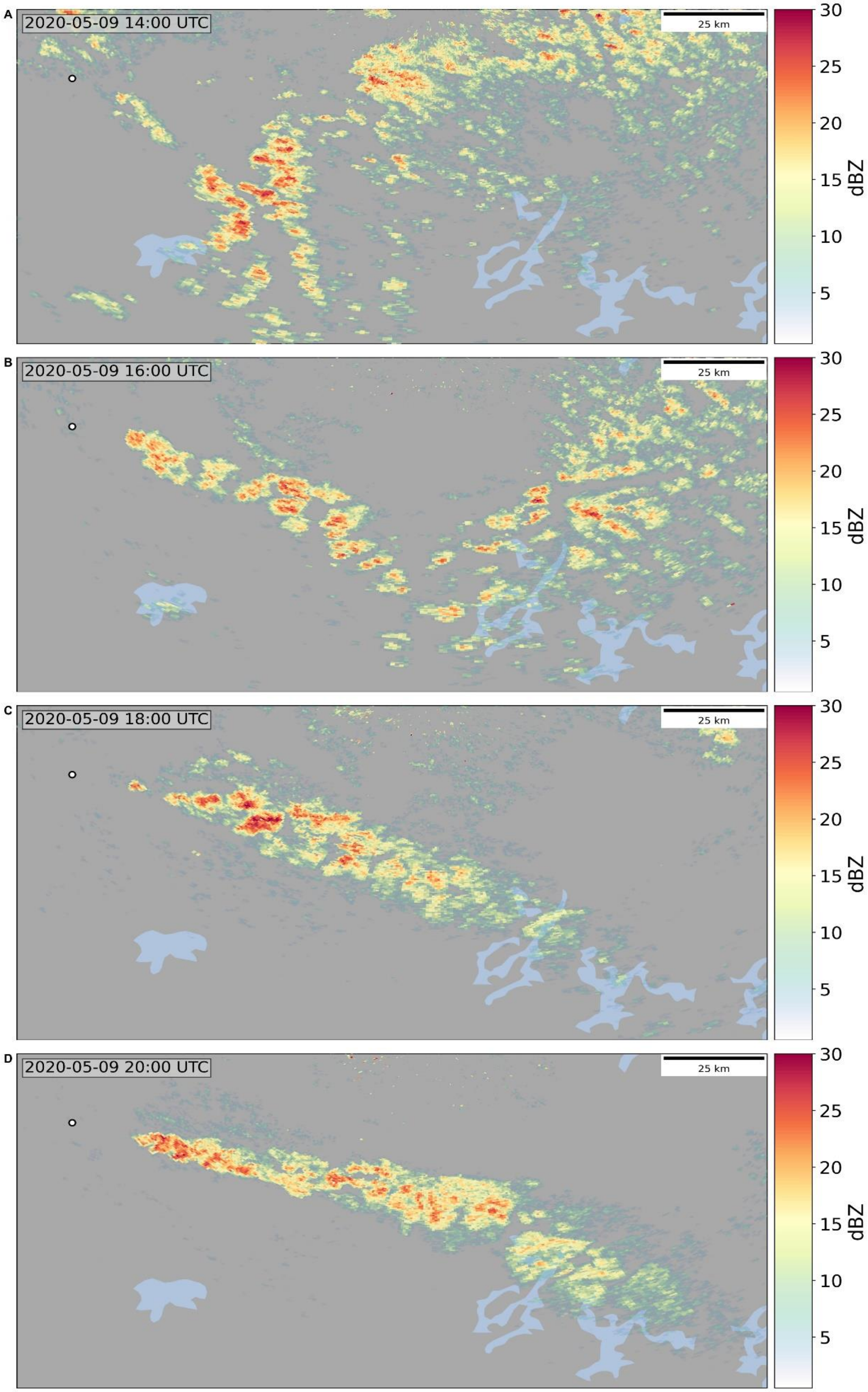
A
2020-05-09 14:00 UTC
25 km
B
2020-05-09 16:00 UTC
25 km
C
2020-05-09 18:00 UTC
25 km
D
2020-05-09 20:00 UTC
25 km
30
25
20
15
10
5
dBZ

Fig. S4.

The temporal evolution of glaciation-induced snow plumes was studied using ground-based precipitation radar data. A glaciation-induced plume of snow is seen in ground-based precipitation radar reflectivity downwind of the copper smelter in Rouyn-Noranda, Canada, on May 9th, 2020, at (**A**) 14 UTC, (**B**) 16 UTC, (**C**) 18 UTC, and (**D**) 20 UTC.

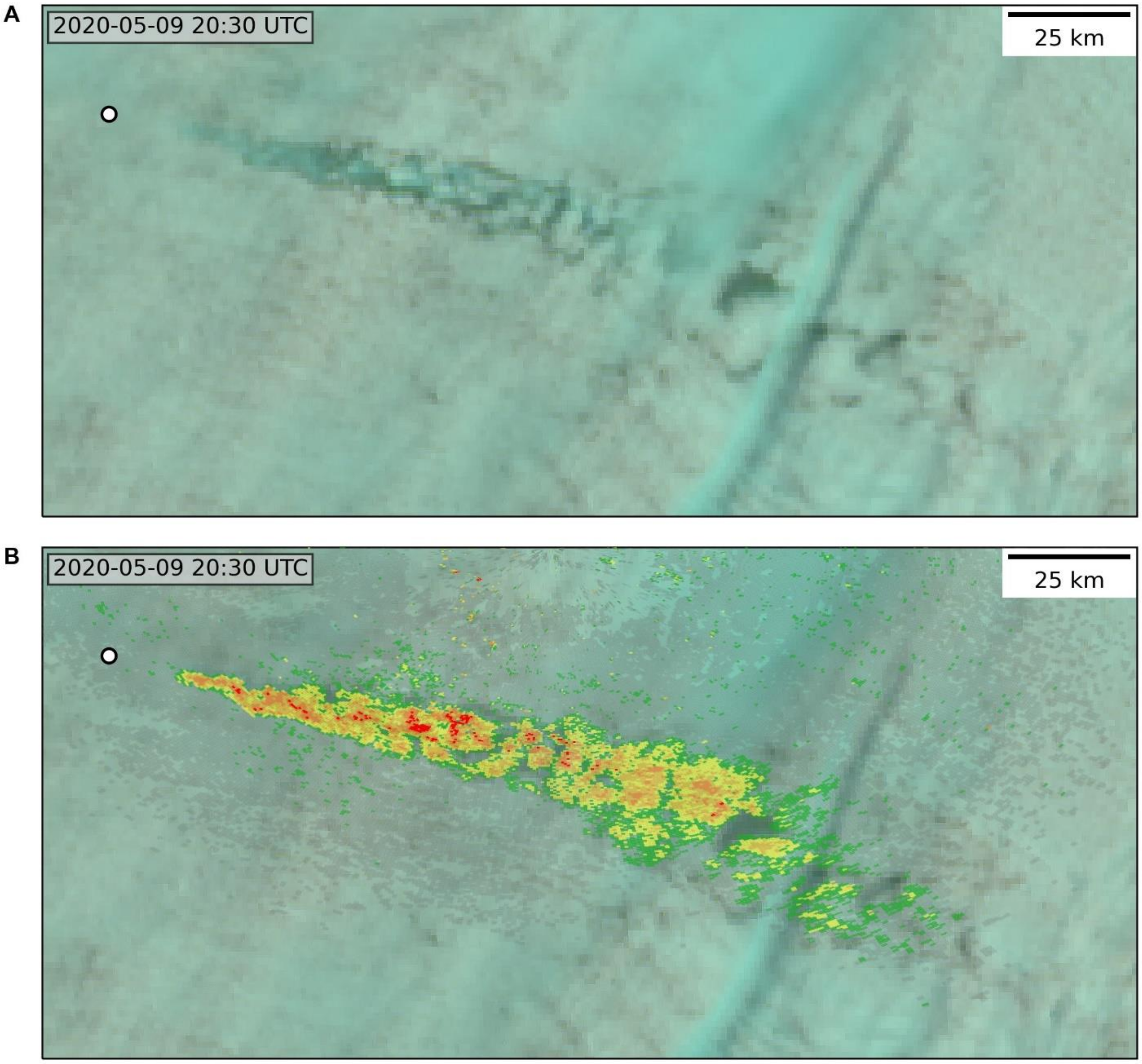

Fig. S5.

The cloud perturbation induced by anthropogenic glaciation that is seen in geostationary GOES ABI satellite data overlaps with the plume of snow seen in ground-based precipitation radar data. (**A**) Glaciation-induced cloud perturbation seen in natural colour composite GOES ABI satellite image downwind of the copper smelter in Rouyn-Noranda, Canada on May 9th, 2020, at 20.30 UTC. (**B**) Overlay of the glaciation-induced plume of snow, seen in ground-based precipitation radar reflectivity, and satellite image for the same glaciation event on May 9th, 2020, at 20.30 UTC.

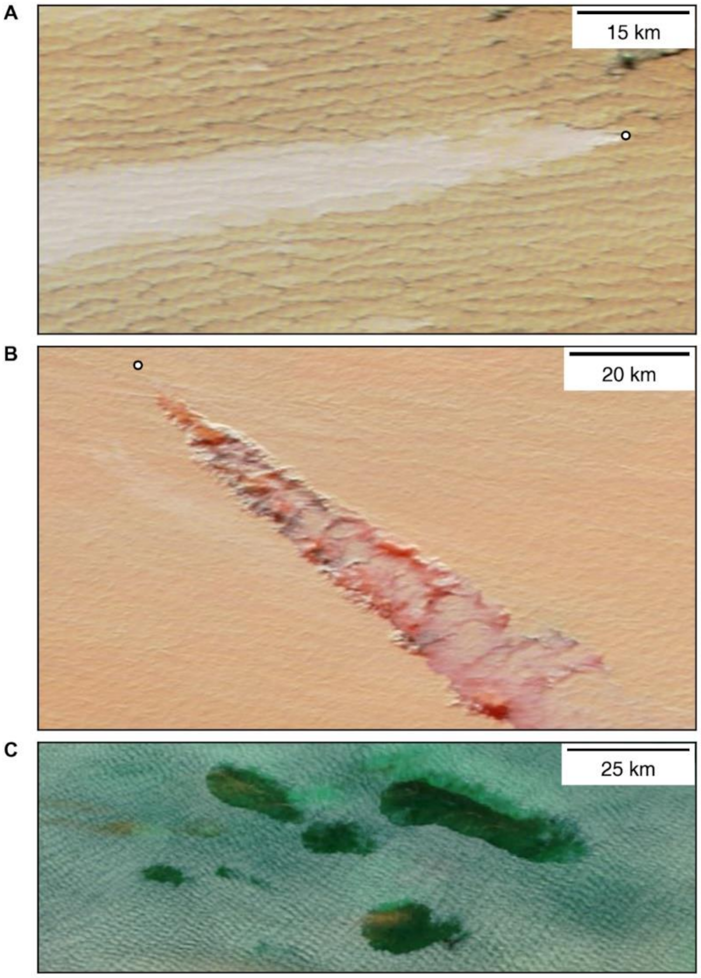

Fig. S6.

Cloud perturbations induced by cloud condensation nuclei (CCN) and glaciation events at industrial aerosol hot spots are visually distinct from aircraft-induced cloud perturbations. Both CCN-induced cloud perturbations (**A**) and glaciation events (**B**) are curvilinear plume-shaped perturbations that follow the shape of the aerosol dispersion plume and often have a characteristic head pointing towards the emission source. **(A)** CCN-induced cloud perturbation downwind of the oil refinery in Kirishi, Russia on October 11th, 2016, and **(B)** glaciation event downwind of the cement plant in Fokino, Russia on January 17th, 2001. (**C**) The shape of aircraft-induced hole punch and canal clouds is usually rounded, as in this example over Texas, USA, on January 29th, 2007, and they do not have a head characteristic of CCN-induced cloud perturbations and glaciation events. Circles mark the locations of anthropogenic aerosol sources.

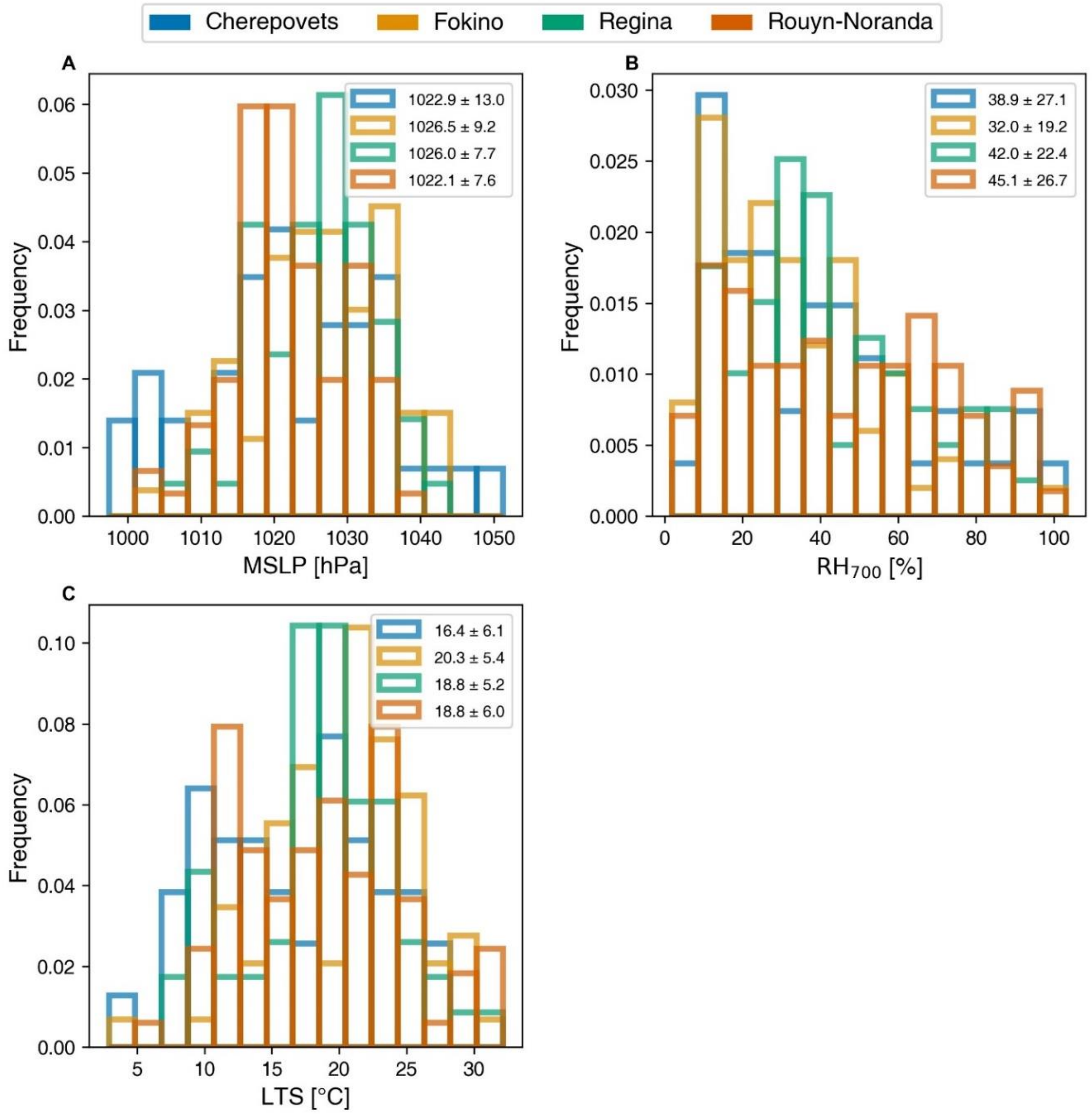

Fig. S7.

Meteorological conditions characteristic of glaciation events based on ERA5 atmospheric reanalysis. (**A**) Mean sea level pressure (MSLP) [hPa], (**B**) relative humidity at 700 hPa pressure level (RH700) [%], and (**C**) lower tropospheric stability (LTS) [°C]. In the legends, the mean values are shown together with the standard deviations.

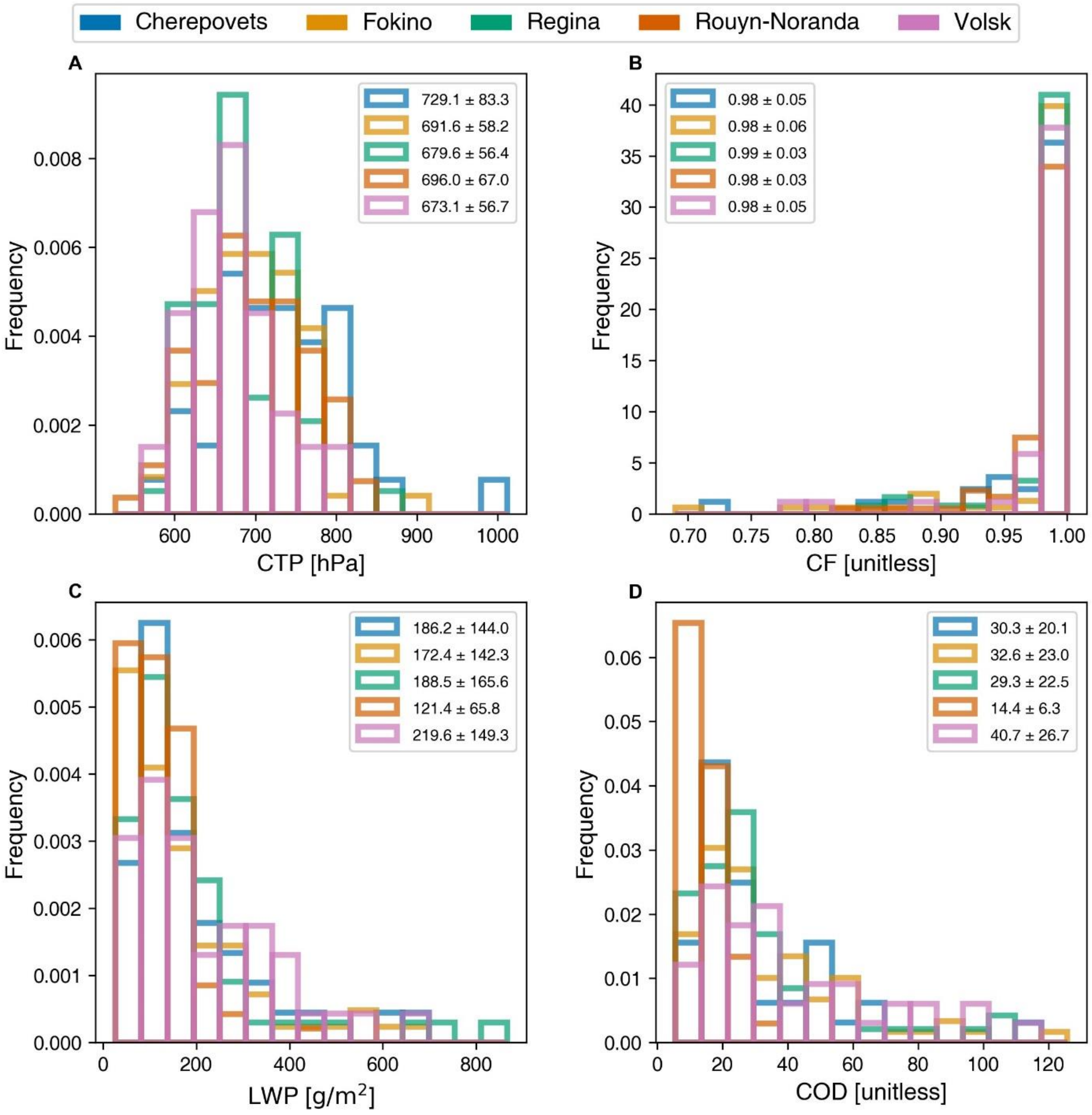

Fig. S8.

Cloud properties characteristic of glaciation events based on MODIS data. (**A**) Cloud top pressure (CTP) [hPa], (**B**) cloud fraction (CF), (**C**) liquid water path (LWP) [g/m^2], and (**D**) cloud optical depth (COD). In the legends, the mean values are shown together with the standard deviations.

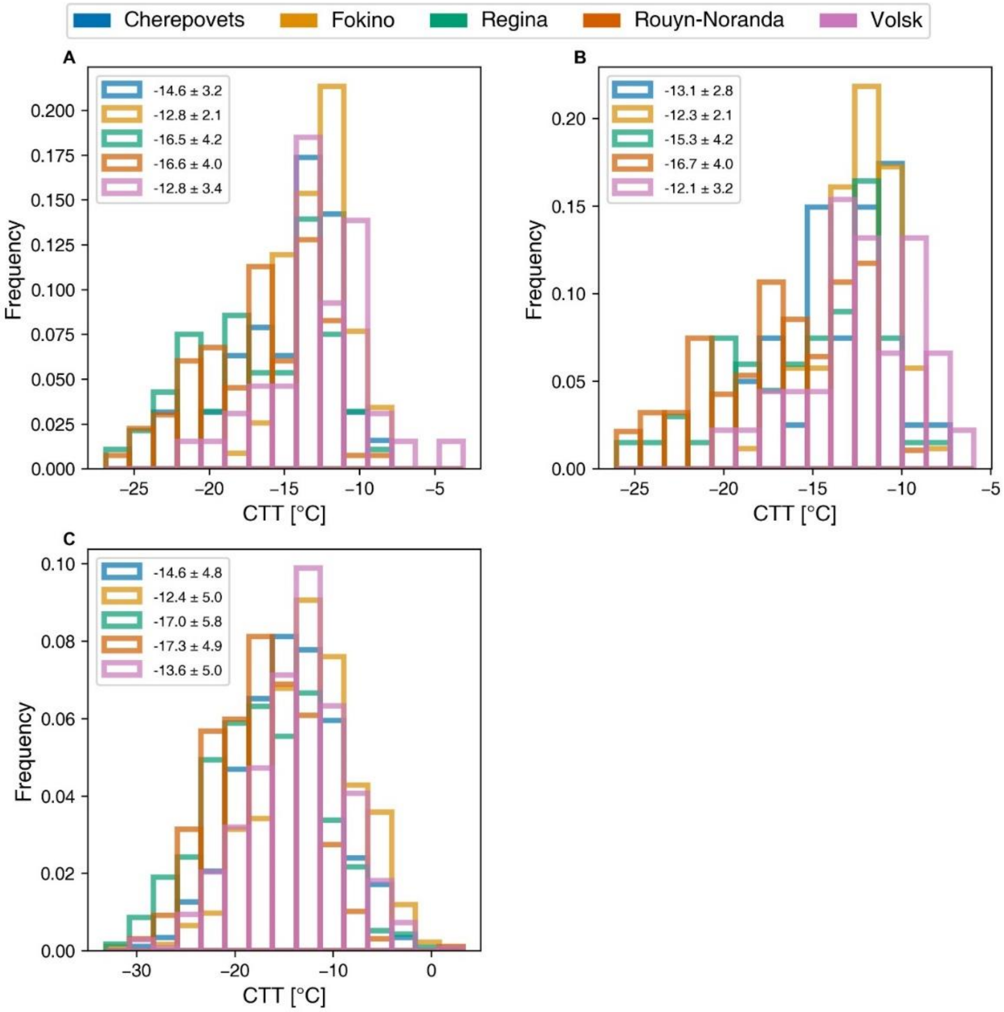

Fig. S9.

MODIS cloud top temperatures characteristic of glaciation events compared to all wintertime supercooled liquid-water cloud decks at the same sites. Cloud top temperatures (CTT) [°C] (**A**) for sampled glaciation events based on Terra MODIS level 2 data, (**B**) for a subset of all glaciation event days based on Terra MODIS level 3 data (1-degree horizontal resolution), the data for days when cloud fraction is equal to or larger than 80%, cloud top pressure is more than 500 hPa, less than 25% of the clouds are ice phase clouds, less than 25% of the clouds are multilayer clouds, and the cirrus fraction is below 25% are shown, and (**C**) for all wintertime supercooled liquid-water cloud decks (December, January, February) clouds based on Terra MODIS level 3 data (1-degree horizontal resolution) for days when cloud fraction is equal to or larger than 80%, cloud top pressure is more than 500 hPa, less than 25% of the clouds are ice phase clouds, less than 25% of the clouds are multilayer clouds, and the cirrus fraction is below 25%. In the legends, the mean values are shown together with the standard deviations.

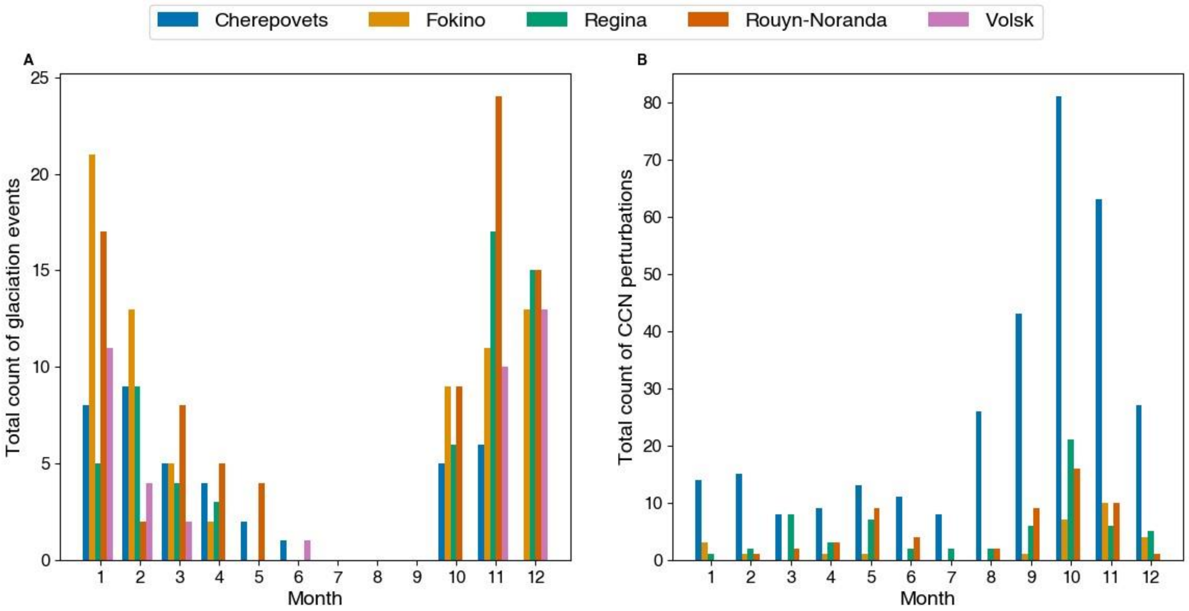

Fig. S10.

Total monthly counts of glaciation events and cloud condensation nuclei (CCN) perturbations on clouds. (**A**) Total monthly count of glaciation events in the years 2000-2021 for each studied site. (**B**) Total monthly count of CCN perturbations in the years 2000-2021 for each studied site.

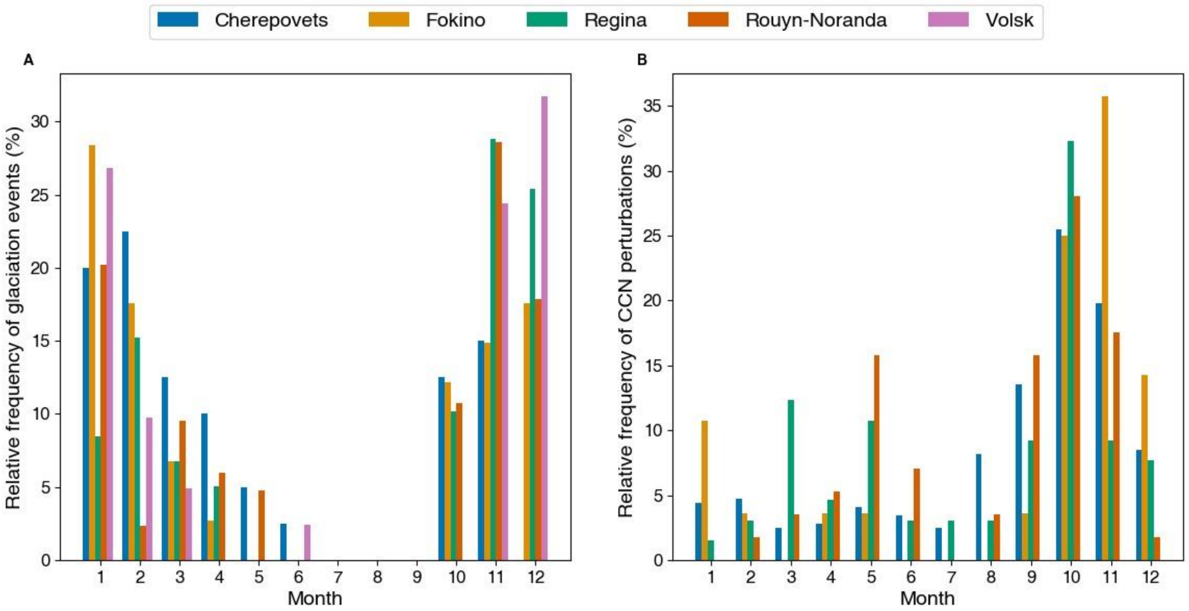

Fig. S11.

Relative monthly frequencies of glaciation events and cloud condensation nuclei (CCN) perturbations on clouds. (**A**) The relative monthly occurrence frequency of glaciation events in the years 2000-2021 for each studied site [%]. (**B**) The relative monthly occurrence frequency of CCN perturbations in the years 2000-2021 for each studied site [%].

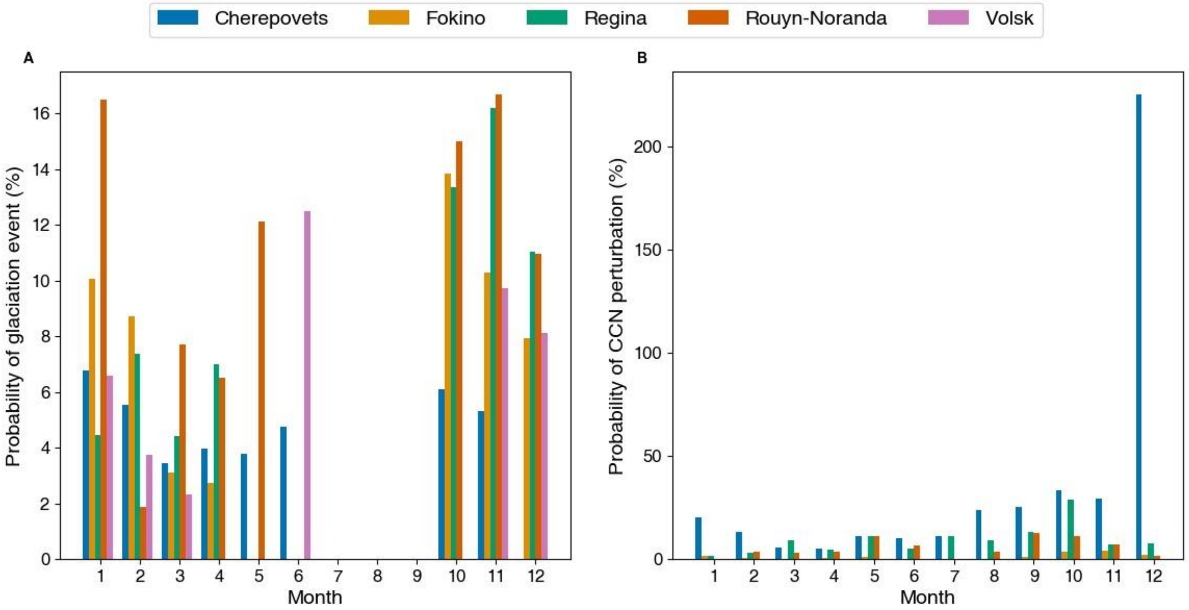

Fig. S12.

Monthly probabilities of glaciation events and cloud condensation nuclei (CCN) perturbations on clouds. (**A**) The ratio of the total monthly number of glaciation event days to the total monthly number of days when a glaciation would be expected for each studied site, multiplied by 100%. We assume that a glaciation event is expected when the cloud fraction is larger than 80%, cloud top pressure is more than 500 hPa, less than 25% of the clouds are ice phase clouds, less than 25% of the clouds are multilayer clouds, the cirrus fraction is below 25%, and cloud top temperatures are between -24 °C and -10 °C in MODIS Terra level 3 daily data (1-degree horizontal resolution) at the studied site. (**B**) The ratio of the total monthly number of CCN perturbations on clouds to the total monthly number of days when a CCN perturbation would be expected for each studied site, multiplied by 100%. We assume that a CCN perturbation is expected when the cloud fraction is larger than 80%, cloud top pressure is more than 500 hPa, less than 25% of the clouds are ice phase clouds, less than 25% of the clouds are multilayer clouds, the cirrus fraction is below 25%, and cloud top temperatures are between -15 °C and 2 °C in MODIS Terra level 3 daily data (1-degree horizontal resolution) at the studied site.

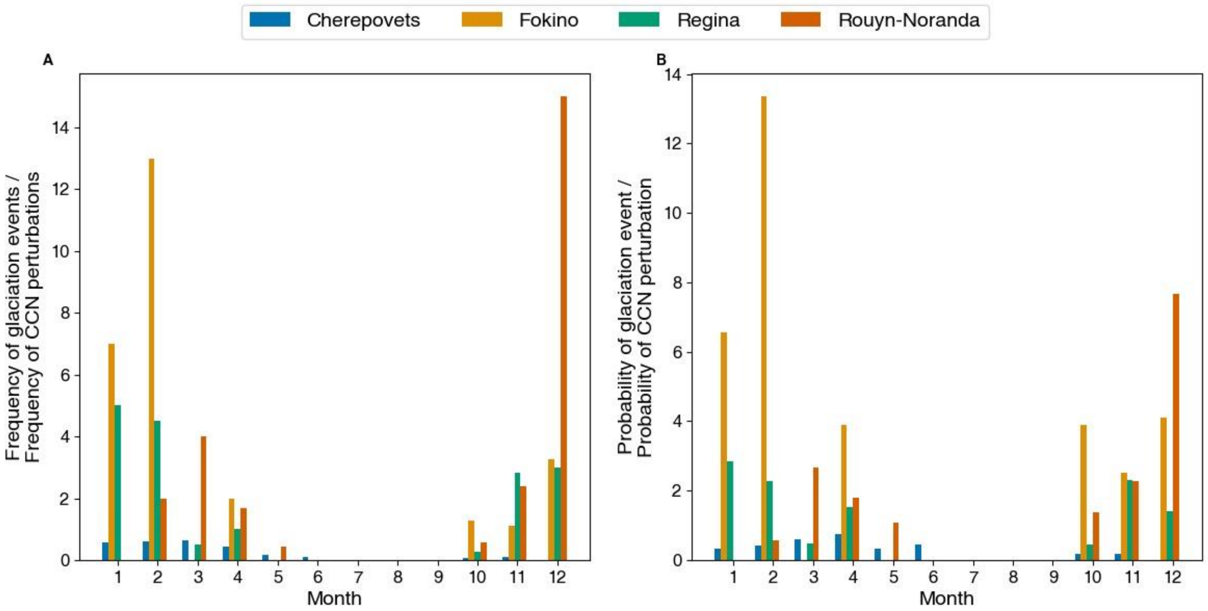

Fig. S13.

The monthly occurrence of glaciation events is divided by the monthly occurrence of cloud condensation nuclei (CCN) perturbations on clouds. (**A**) The total monthly count of glaciation events (Fig S10a) is divided by the total monthly count of CCN perturbations (Fig S10b) for each studied site. (**B**) The monthly probability of glaciation events (Fig S12a) is divided by the monthly probability of CCN perturbations (Fig S12b) for each studied site.

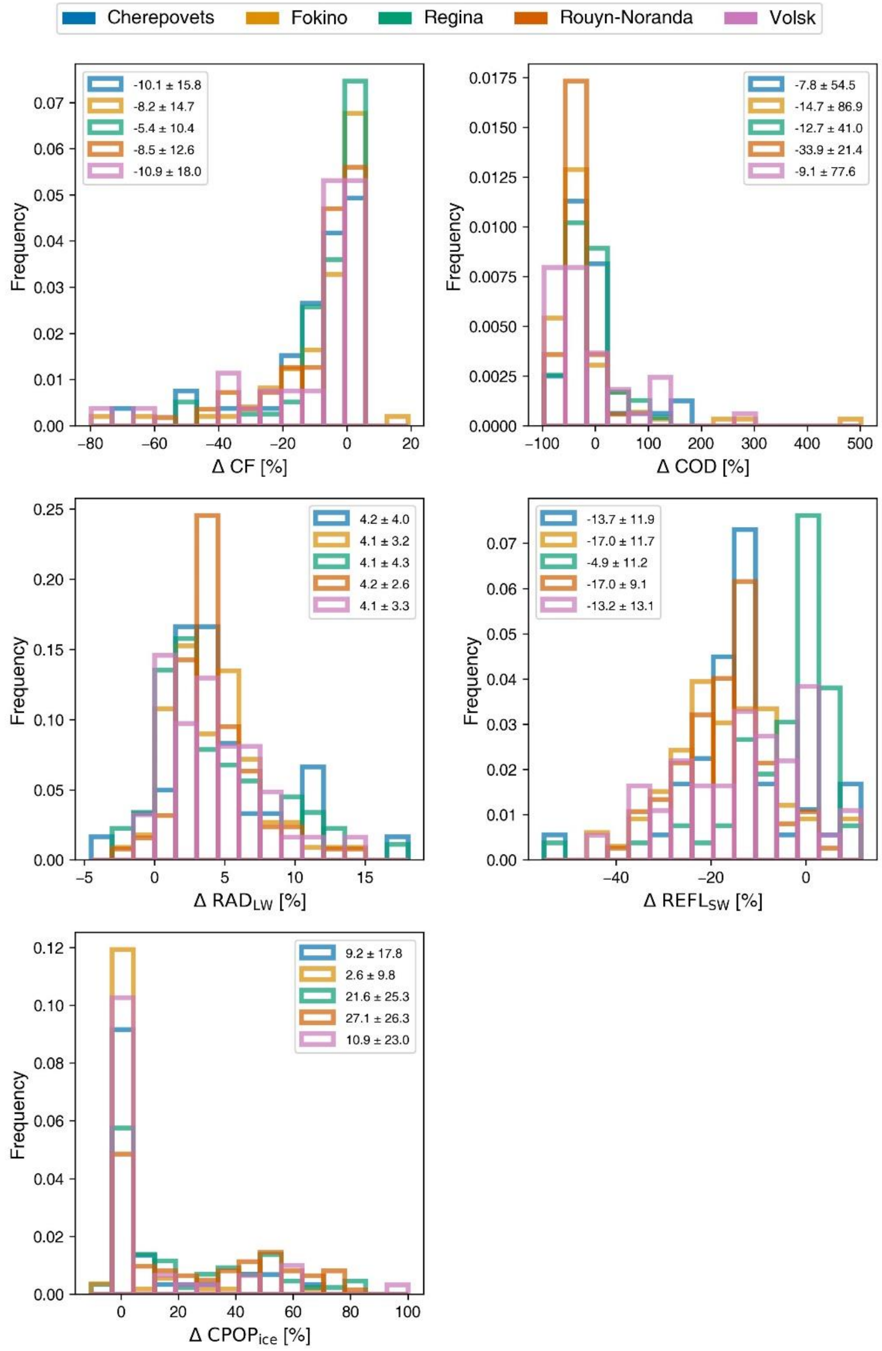

Fig. S14.

Anthropogenic glaciation of supercooled liquid-water clouds influences cloud properties. Fractional changes in cloud fraction (CF), cloud optical depth (COD), shortwave reflectance at 0.545 to 0.565 µm (REFL$_{\mathrm{SW}}$), and longwave radiance at 10.78 to 11.28 µm (RAD$_{\mathrm{LW}}$), and the differences in the fraction of ice-phase pixels in the glaciation-affected areas based on Cloud Phase determined by the Optical Properties algorithm (CPOP$_{\mathrm{ice}}$; *24*), compared to nearby unaffected areas based on MODIS data. In the legends, the mean changes are shown together with the standard deviations.

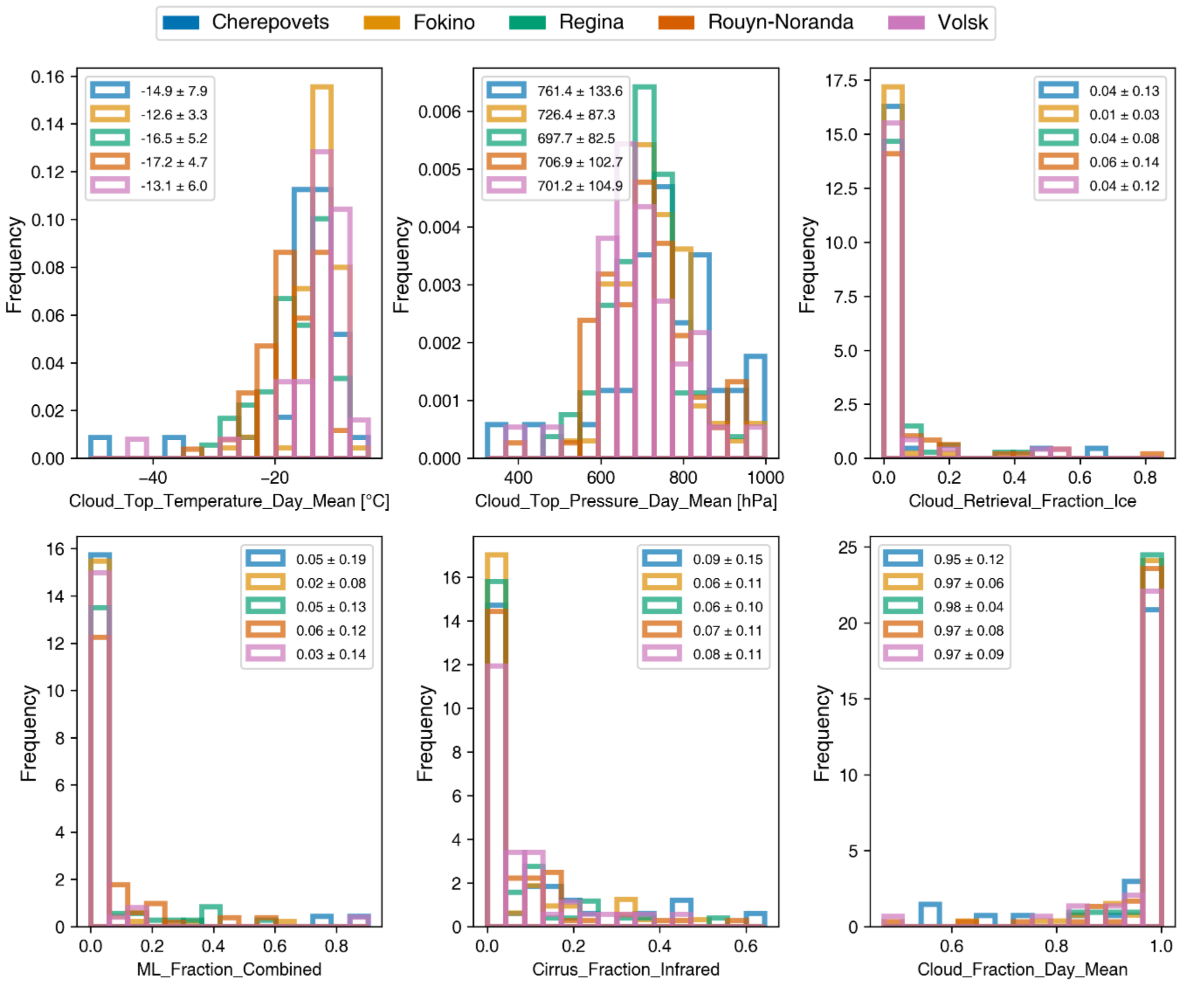

Fig. S15.
Cloud properties characteristic of glaciation event days from MODIS level 3 daily data. We use the nearest gridpoint from level 3 data to characterize cloud top temperatures (Cloud_Top_Temperature_Day) [°C], cloud top pressure (Cloud_Top_Pressure_Day_Mean) [hPa], fraction of ice clouds (Cloud_Retrieval_Fraction_Ice), fraction of multilayer clouds (ML_Fraction_Combined), fraction of cirrus clouds (Cirrus_Fraction_Infrared) and cloud fraction (Cloud_Fraction_Day_Mean) for glaciation event days for each pollution source. These distributions inform the selection of thresholds to select all days that are potentially favourable for the occurrence of glaciation events at industrial aerosol hot spots.

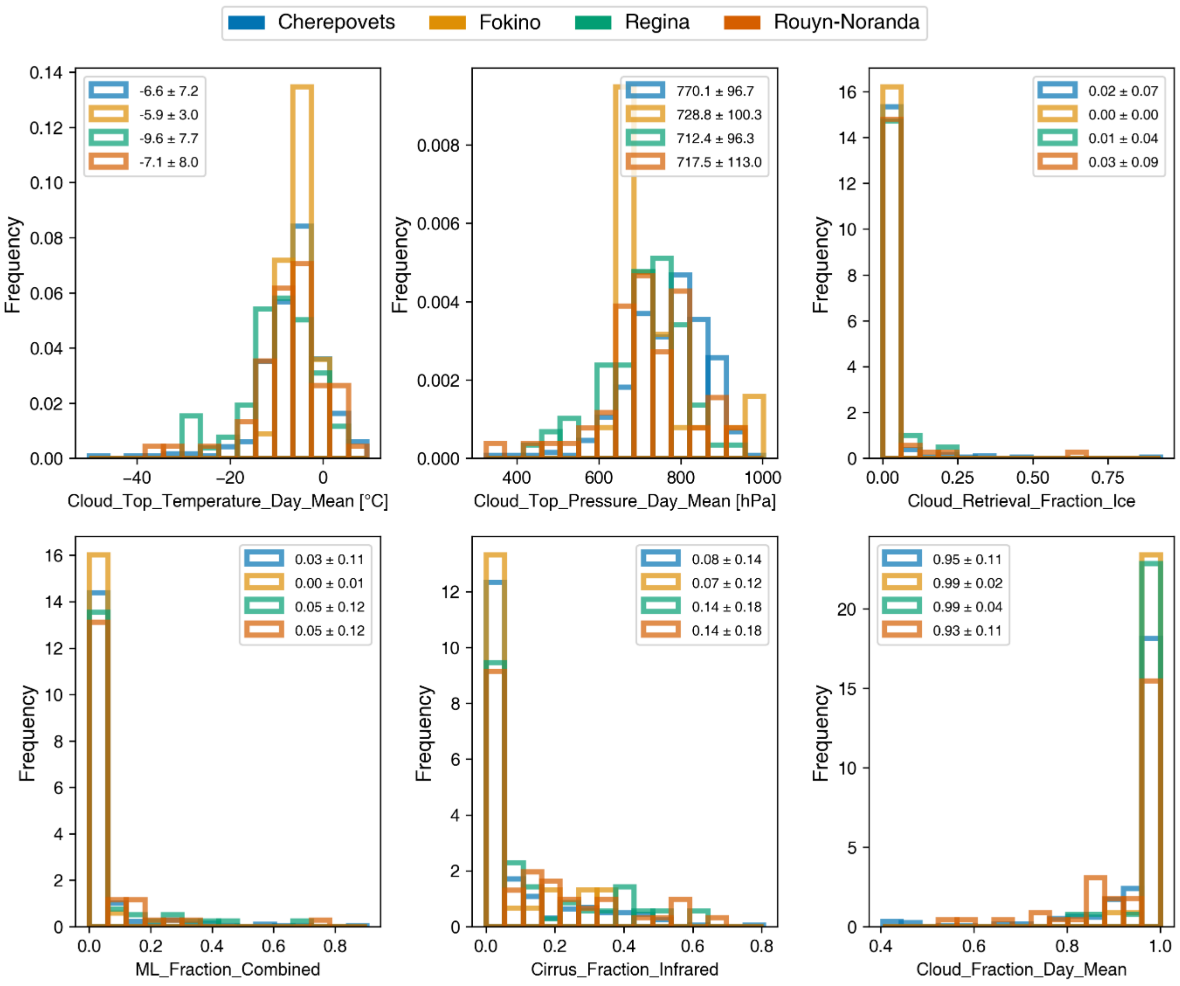

Fig. S16.

Cloud properties characteristic of CCN perturbation days from MODIS level 3 daily data. We use the nearest gridpoint from level 3 data to characterize cloud top temperatures (Cloud_Top_Temperature_Day) [°C], cloud top pressure (Cloud_Top_Pressure_Day_Mean) [hPa], fraction of ice clouds (Cloud_Retrieval_Fraction_Ice), fraction of multilayer clouds (ML_Fraction_Combined), fraction of cirrus clouds (Cirrus_Fraction_Infrared) and cloud fraction (Cloud_Fraction_Day_Mean) for CCN perturbation days for each pollution source. These distributions inform the selection of thresholds to select all days that are potentially favourable for the occurrence of CCN perturbations on clouds at industrial aerosol hot spots.

Movie S1.

The temporal evolution of glaciation events in supercooled clouds was studied using geostationary satellite data. GOES ABI animation of a plume-shaped glaciation event downwind of the copper smelter in Rouyn-Noranda, Canada on November 18th, 2020. (**A**) 3.9 µm channel data, (**B**) night microphysics composite, (**C**) natural colour composite and (**D**) day microphysics composite.

Movie S2.

The cloud perturbation induced by anthropogenic glaciation that is seen in geostationary GOES ABI satellite data overlaps with the plume of snow seen in ground-based precipitation radar data. (**A**) Glaciation-induced cloud perturbation seen in natural colour composite GOES ABI satellite images downwind of the copper smelter in Rouyn-Noranda, Canada on May 9th, 2020. (**B**) Overlays of the glaciation-induced plume of snow, seen in ground-based precipitation radar reflectivity, and satellite images for the same glaciation event.

Movie S3.

The temporal evolution of glaciation-induced snow plumes was studied using ground-based precipitation radar data. A glaciation-induced plume of snow is seen in ground-based precipitation radar reflectivity downwind of the copper smelter in Rouyn-Noranda, Canada, on May 9th, 2020.